5-2011

New Interfacial Nanochemistry on Sensory Bioscaffold-Membranes of Nanobelts

Feng Chen
University of Arkansas, Fayetteville

New Interfacial Nanochemistry on Sensory Bioscaffold-Membranes of Nanobelts

New Interfacial Nanochemistry on Sensory Bioscaffold-Membranes of Nanobelts

A dissertation submitted in partial fulfillment
of the requirement for the degree of
Doctor of Philosophy in Chemistry

By

Feng Chen
National University of Defense and Technology
Bachelor of Science in Applied Chemistry, 1986

May 2011
University of Arkansas

ABSTRACT

Nanostructured bioscaffolds and biosensors are evolving as popular and powerful tools in life science and biotechnology, due to the possible control of their surface and structural properties at the nm-scale. Being seldom discussed in literature and long-underexploited in materials and biomedical sciences, development of nanofiber-based sensory bioscaffolds has great promises and grand challenges in finding an ideal platform for low-cost quantifications of biological and chemical species in real-time, label-free, and ultrasensitive fashion.

In this study, titanate nanobelts were first of all synthesized, from hydrothermal reactions of a NaOH (or KOH solution) with TiO_2 powder, to possess underexploited structure and surface vital to the rapid and label-free electrochemical detections of protein (cytochrome c) and neurotransmitter (dopamine). This work is based on a suite of new physical and chemical properties on the titanate nanobelt in water, including high surface area, zwitterionic surface, chemical- and photochemical-durability, cation-exchange and anion- and cation-sorption capacities, protein- and cell-compatibility, thermal-stability, and charge conductivity.

The Fourier transform infrared (FTIR) was used for identifying any denaturing of the cytochrome c pre-immobilized on the titanate nanobelts. On that basis, the pheochromocytoma cells (PC-12 cell) were chosen to grow on the titanate nanobelts. These experiments prove that the sensory bioscaffolds of titanate nanobelt-membrane is a multiplex platform for developing new tools for energy, environmental and life sciences.

This dissertation is approved for
Recommendation to the
Graduate Council

Dissertation Director:

_____

Dr. Z. Ryan Tian

Dissertation Committee:

_____

Dr. Jingyi Chen

_____

Dr. Derek Sears

_____

Dr. Bill Durham

DUPLICATION RELEASE

I hereby authorize the University of Arkansas Libraries to duplicate this dissertation when needed for research and /or scholarship.

Agreed _____

Feng Chen

Refused _____

Feng Chen

ACKNOWLEDGEMENTS

I give the special appreciation to the Lord who is taking care of me.

I would like to thank my advisor, Professor Z Ryan Tian, for providing me opportunities to learn nanomaterial's syntheses, characterizations and applications in his Lab, and for encouraging me to become a good scientist.

I greatly appreciate Professor Bill Durham for his endless help without which I would never have finished my PhD, and Dr. Sears, Dr. Li, and Dr. Jingyi Chen for inspiring me to do research independently. I give special thanks to Prof. J. Li who offered me a wonderful opportunity to work at NASA Ames Research Center in California, and to Drs. Charles L Wilkins, Jack Lay and Rohana Liyanage who kindly taught me the mass spectrometry.

Many thanks to staff members on campus including Drs. Wenjun Dong, Tierui Zhang, Jining Xie, Myeong Lee, and Huajun Zhou for their kind assistances in my graduate researches, and to group members in Dr. Tian's lab for helping and encouraging me throughout my studies in the lab. I would like to thank Professor Xiaogan Peng and his group members including Drs. Yongfen Chen and Mike Rutherford for helping me in my FTIR and TGA experiments.

Special Thanks to my parents, my husband, and my son for always being there to support me and encourage me.

TABLE OF CONTENTS

LIST OF FIGURES

LIST OF SCHEMES

LIST OF ABBREVIATIONS

2D	Two-dimensional
3D	Three-dimensional
AFM	Atomic force microscopy
Cyt.c	Cytochrome c
DA	Dopamine
DDI	Distilled deionized
DPV	Differential pulse voltammetry
e	electron charge (1.6×10^{-19} C)
E	Applied potential
E^o	Formal potential
ΔE	Difference of the peak potentials
E½	Half peak potential
EDX	Energy dispersive x-ray
E_p	peak potential
E_{pa}	Anodic peak potential
E_{pc}	Cathodic peak potential
FET	Field-effect transistor
FTIR	Fourier transformation infrared spectroscope
GE	Graphite electrode
k	The Boltzman constant
PC-12 cells	Pheochromocytoma cells
QD	Quantum Dots

RE	Reference electrode
RT	Room temperature
SAM	Self-assembled monolayer
SEM	Scanning electron microscopy
SWV	Square wave voltammetry
TGA	Thermogravimetric analyses
T	absolute temperature
TEM	Transmission electron microscopy
WE	Working electrode
XRD	X-ray diffraction
ψ_0	the surface potential

PART I. INTRODUCTION

Chapter 1.

Overview of Nanostructured Biomaterials

1.1. Nanostructured Fibrous Materials

One-dimensional (1D) nanomaterials usually refer to nanostructured fibrous materials including nanorods, nanobelts and nanotubes, each with one dimension between 1 and 100 nm. These nanomaterials, compared to their bulk counterparts, can offer unique opportunities for developing new devices in important applications ranging from space exploration to our daily life. For example, carbon nanotubes have been used in air revitalization to reduce the system-volume and increase the working efficiency for space-shuttle. [1]

In recent years, enormous numbers of new properties and structures for a large variety of 1D nanomaterials (e.g. nanowire[2,3,4] and carbon nanotubes[5]) have been exploited in search for new nanotechnologies. However, developments of truly industry-viable nanotechnologies for advancing, especially, aerospace, energy, environmental, and life sciences still possess some long-unmet challenges. Much of the problems are due to the lack of understanding and control of interfacial properties at the nanoscales, especially at the nanomaterials-water interface. Growing demands for removing these technological roadblocks have been inspiring people worldwide to work hard on studying new basic and applied nanoscale interfacial properties along with developing new 1D nanomaterials. In

this end, there will be a growing need for exploiting new interfacial nanochemistry, and in turn for design and development of the new 1D nanomaterials and nanotechnologies.

1.2 Neuron-regenerative Nanofibrous Bioscaffolds

Nanomaterials in biomedical applications have been extensively studied lately because of their tremendous potentials in developing new drug delivery mechanisms and tissue engineering scaffolds,[6,7] on the basis of their unique nanoscale physical, mechanical, and chemical properties. These bionanomaterials are required to mimic the cellular microenvironment in biological systems and to provide the properties including biocompatibility, programmable degradability, inert immunity, high porosity, and low-cost.

Recent advances in bionanomaterials science offer a broad range of promising applications in neural tissue-engineering including promoting brain-protection and repairing neural regeneration.[8,9] The advancement of the regenerative neural science has imposed a great demand for highly selective nanofibrous bioscaffolds due to the neuron-cell's vulnerability to the environment change. To achieve this goal, numerous strategies for developing new fabrication processes and achieving desired properties have been investigated for DNA-, protein-, and polymer-based nanofibrous bioscaffolds. These synthetic nanofibrous bioscaffolds have been found good for neural tissue engineering because their properties are analogous to the natural extracellular matrix (ECM) in supporting the neuron-regenerative processes.

1.2.1 Nanofibrous Scaffolds as Extracellular Matrix Analogues.

The nanofibrous scaffolds provide a promising framework to support cells in neural reconstruction.[10,11] The surface of nanofibrous scaffolds can be modified by native extracellular matrix (ECM) proteins and nucleic acids to offer the suitable microenvironment for promoting cell adhesion, proliferation, differentiation, and growth.[11,12,13]

The desired self-assembling peptide nanofiber bioscaffolds have been successfully implanted into the lesion site in the hamster superior colliculus and physically mimicked the ECM.[14] This bioscaffold consists of entangled nanofibers which were made through ionic L-amino acid and self-assembled highly hydrated scaffolds in the presence of physiological solutions. The experimental results illustrated that the bioscaffolds provided the permissive environment, and not only significantly regenerated the axons but also reconnected the disconnected damaged brain tissue. The specific structure of this bioscaffold connected the two extents of the lesion, and then the cells could move into the scaffold. This promoted the interaction between the scaffolds and the ECM and neural tissue on both sides of the lesion cavity.

Other strategies for fast neurite outgrowth used a nanofibrous scaffold functionalized with bioactive molecules such as ECM proteins, neuroactive peptides and growth factors. Laminin, one of the ECM proteins, has been incorporated with poly (L-Lactic acid) (PLLA) nanofiber by electrospinning procedure.[15] This modified nanofibrous scaffold created the biomimic environment and promoted cell adhesion, proliferation, and differentiation. The

aligned PLLA nanofibrous scaffold immobilized with laminin and basic fibronectin growth factor using di-amino poly(ethylene glycol) as connector which enhanced the bioactivities of the bioscaffold and promoted and guided the neurite outgrowth.[16]

Many studies have demonstrated that neural behaviors have been affected by the various nanoscale morphologies and the microscale alignments of nanofibrous scaffolds produced by electrospinning.[16] The aligned electrospun nanofibrous scaffold served as nerve guidance channels and could direct the dorsal root gangia (DRG) neurite growth compared with intermediate and random aligned scaffolds.[17] The DRG neurite growth on nanofibrous scaffolds coated with laminin in different orders, structures, and surface properties has been extensively studied.[18] The results demonstrated that the DRG neurite outgrowth expressed either the aligned or random neurite fields depended on the orientation of the underlying nanofibers.

1.2.2 Growth of Neural Stem Cell and Nanofibrous Scaffolds

The nanofibrous scaffolds could be used as the substrate to support neural stem cells for brain repair. This is because the desired nanofibrous scaffolds promoted the attachment, growth, and differentiation of neural stem cells. Many strategies to modify and functionalize the scaffolds include the change of the surface morphologies, modification of the surface with bioactive molecules, and variation of the cell seeding densities.

The mouse embryonic stem cells (ESCs) have been seeded on both random and aligned nanofibrous scaffolds modified with retinoic acid.[19] The significant results demonstrated that the aligned nanofibrous scaffolds not only enhanced the differentiation of ESCs into neural lineage cells but also guided the direction of neuritis outgrowth, in comparison to the random nanofibrous scaffolds. The proliferation and differentiation of neural stem cells (NSCs) could be affected by various biochemical and topographical cues.[20] The rat hippocampus-derived adult NSCs have been cultured on the nanofibrous and microfibrous polyethersulfone (PES) scaffolds coated with laminin. The rat NSCs represented less cell spreading, migration, and proliferation with increasing diameters of nanofibrous scaffolds under the proliferation condition (serum free medium and fibroblast growth factor-2 (FGF-2). The results also demonstrated that the rat NSCs had a faster proliferation rate and a higher percentage of proliferative rat NSCs on a two dimensional (2D) substrate compared with that on the increasing diameters of nanofibrous scaffolds. Under the differentiation condition (1 mM retinoic acid and 1% fetal bovine serum (FBS), the rat NSCs differentiated into oligodendrocytes on the 2D substrate and smaller diameters' nanofibrous scaffolds. For large diameter scaffolds, they differentiated into neuronal lineage. These evidences suggested that the topographical cues of nanofibrous scaffolds and biochemical conditions have great influenced the differentiation and the proliferation on the stem cells.

The surface modifications of nanofibrous scaffolds with bioactive molecules physically mimicked the architecture of the extracellular matrix and

offered opportunities for guiding and promoting the neurite outgrowth. The desired composition, morphology, and structure of the nanofibers could impact the cellular adhesion, spreading, migration, proliferation, and lineage specification as applied in conjunction with targeted biochemical signals. These results suggested the nanofibrous scaffolds have significant potential in application to the neural tissue engineering.

1.3 TiO_2-based Nanostructured Biomaterials

Titanium dioxide (TiO_2) has been widely used in photocatalysis,[21, 22] catalysis,[23] hydrogen storage,[24] and lithium battery.[25,26] TiO_2 nanomaterials have emerged as a very useful nanomaterials because of their unique chemical and physical properties. These include a large surface area, optical transparencey, low-toxicity, high thermal stability, and chemical and photochemical stabilities.

1.3.1 Syntheses of TiO_2–based Nanostructured

To synthesize TiO_2 nanostructured materials, the main methods are template synthesis, electrochemical synthesis, and hydrothermal syntheses. The template synthesis includes a polymer mold,[27] direct deposition technique,[28] sol-gel template preparation,[29] supermolecular assembled processes,[30] and sol-gel coating.[31] The electrochemical synthesis includes direct anodization of Ti foil in an H_2O–HF electrolyte at room temperature.[32] The other fluoride-ion-containing electrolytes were also available for this purpose.[33,34] The products of template and electrochemical synthesis were TiO_2 nanotubes. For the alkaline

hydrothermal synthesis, the raw TiO_2 powder reacts with high concentrations of 10M NaOH (or KOH) solution at various temperatures (60─ 240 ºC) and can be converted titanate nanomaterials such as nanoparticles, nanotubes, and nanobelts/nanoribbons. The nanostructure of the products depends on the temperature and time. Based on the examination of transmission electron microscopy (TEM), scanning electron microscopy (SEM), and x-ray diffraction (XRD) data, the crystal structure of titanate nanomaterial consists of layered TiO_6 edge and corner sharing octahedron and cations separated between layers.[35, 36]

1.3.2 Properties and Applications of TiO_2–based Nanomaterials

The thermal stabilities were different for nanofibers and nanotubes. During calcination, Na-titanate nanofibers were consecutively transformed to TiO_2-B at 400 ºC, anatase at 700 ºC, and rutile at 1000 ºC, and then the nanofibrous morphology disappears.[36] The Na-nanotubes was stable until 600 ºC, but it changed to TiO_2-B with some rutile after heating over 800 ºC.[35] It was found that the amount of sodium cations separated between the interlayers affected the thermal stability of titanate nanotube.

The absorption and magnetic properties could be changed through intercalating Fe atom into proton (H^+) titanate nanotubes ($H_2Ti_3O_7$) under hydrothermal synthesis.[37] The experimental result showed the improved efficiency of photoabsorpation because the absorption edge was shifted from ultraviolet to the visible region after doping Fe into the nanotubes. It was supported by the theoretical calculation which demonstrated that the band gap of

Fe intercalated titanate nanobelts decreased dramatically compared with that of titanate nanobelts because of introducing the inter gap band. The magnetic property of also changed based on the inter gap band.

The layered titanate nanomaterials have the property of cation intercalation. The process of ion exchange had been studied by using alkali metals cation[38] and transition-metal ions.[39] The interlayer distance of the nanotube was unchanged after intercalating with alkali metal cations (Li, Na, K, Rb, Cs) in aqueous solution.[38] The optical and magnetic properties can be modified by intercalating with different transition-metal cations (Cd^{2+}, Zn^{2+}, Co^{2+}, Ni^{2+}, Cu^{2+}, Ag^{+}) by stirring the nanotubes in the transition-metal solutions.[39] The H^{+} may intercalate with other alkali and transition cations, but it found that the reversed reaction was difficult.

For photocatalysis application, both H-titanate nanofibers and its composite structure, H-titanate nanofiber covered with anatase nanocrystals, had photocatalytic activity. The synthetic dyes degraded this photoactivity under UV light irradiation.[40] After decorating with CdS nanoparticles, the cation exchanged titanate nanotubes demonstrated the photochemical activity.[41]

The titanate nanotubes synthesized through hydrothermal reaction showed good catalytic properties and was a novel, inert, and versatile substrate for both inorganic and biomolecules.[42] The Ru(III) hydrated oxide highly loaded on both the inner and outer surface of the titanate nanotubes and exhibited the selective oxidation of alcohols. The catalyst of Ru(III)/nanotube demonstrated high

selectivity and improved activity compared with Ru(III)/Al_2O_3, and good stability.[43]

Developing new advanced materials for hydrogen storage is one of the most challenging barriers for researchers because hydrogen can be used as an energy carrier, hydrogen fuel cell, and an environmentally clean energy. The TiO_2 nanotubes were found to reproducibly store hydrogen up to ~2 wt% at room temperature and 6 MPa.[43] The 75% of stored hydrogen from physisorption can be released at ambient pressure. The 13% stored hydrogen weakly chemisorbed could be released at 70ºC. The other 12% is hydrogen bonded to oxide ions as water and can be released at 120ºC. A similar result was found that hydrogen was reversibly accumulated on the multilayer titanate nanotube through sorption in the temperature range from -195 – 200ºC and pressure from 0 – 6 bar.[44]

1.4 Multifunctional Membrane of Zwitterionic Titanate Nanobelts

The unique chemical and physical properties of nanostructured materials have attacked novel attentions today due to the emerging applications in the life science and medicine,[45, 46, 47, 48] photocatalysis,[49] solar cell,[50] lithium batteries[51, 52] and self-powered nanosystems.[53] The diameter of nanobelts[54] and /or nanowires is compatible with biological molecules, protein and viruses. The label-free and direct detection of single viruses using functionalized silicon nanoire has been first achieved in Liber's group.[55] The real-time and selective measurements of multiple cancer marker proteins on functionalized silicon nanowire surface[45] have been developed in recent years. The remarkable example for multifunctional

semiconductor quantum dots was that used in cancer targeting and imaging in *vivo* conditions.[48]

Layered nanostructured titanate provided the opportunities to change the electrical conductivity, magnetic and optical properties through controlling the composition and crystal structure.[56, 57, 58] The intensity of photoluminescence was dramatically increased by using cation (Na^+) exchanged layered titanate nanosheets.[56] The cation size and location in the interlayer space were believed the major influenced parameters that changed the electronic and geometric structure of the [TiO_6] octahedron. The transition-metal ions of Fe and Ni intercalated into layered titanate nanotube $H_2Ti_3O_7$, the band gap of the Fe- and Ni- intercalated titanate nanotube were considerably shifted to the visible region.[57] The experiment data was agreed with simulation model in this experiment. From the calculating electron density maps, the researchers found the band gap was reduced based on the overlapping the 3d electrons of transition-metal cation of Fe or Ni in the interlayer with electron clouds of two [TiO_6] octahedral layers.

The selectively chosen cation to functionalize the nanostructure titanate may change the physical property of nanomaterials such as magnetism.[58] After intercalating the transition-metal ion Co^{2+} to the titanate nanotube ($Na_xH_{2-x}Ti_3O_7$) by simply stirring in the ammonia solution at room temperature, the Co-substituted titanate nanotube was converted to the magnetic semiconductor.

The layered titanate nanobelt is promising in rechargeable lithium batteries due to its unique layered lattice and cation exchangeable property. To

improve the capacity of rechargeable lithium batteries, the intercalation of lithium cation into layered nanostructured titanate was developed.[59, 60] The electrode using lithium cation intercalated titanate Nanobelt exhibited high discharge/charge rate capacity, large lithium intercalation capacity, and great cycling stability.

To develop the electrochemical sensors for chemical and biological targets, the sensitivity and selectivity of electrodes are the most important parameters that have challenge to improve. The modified electrodes for electrochemical sensing have been used to reach the required goals.[61,62,63,64,65,66] The ideal structure and properties of material for modified electrode to detect biological targets are biomembrane-like, biocompatibility, and minimized degradation during the monitoring. The sensitivity and selectivity are enhanced at same time.

The heme protein cytochrime c (cyt.c) has been widely investigated since the function of cyt. c is a mobile shuttle for electron transition from cytochrome bc_1 complex to cytochrome oxidase in the mitochondrial respiratory chain.[67] To study electron transfer of cyt.c, the modified electrodes using conducting polymer, carbon nanotube, and clay materials have been developed.[68,69,70] Compared with conducting polymer, carbon nanotube, and clay materials, the nanostructured titanate has the advantages of intrinsic structure and properties as mentioned before.

Chapter 2.

Overview of Biosensors Based on 1D Nanostructures

2.1 Biosensors Based on 1D Nanostructures.

Nanostructured sensors (e.g. silicon nanowire- and carbon nanotube-based sensors) are being explored as new and potential tools for studying medicine and life sciences. Silicon-nanowire sensors offer a powerful and general platform for direct, ultrasensitive and real-time detections in future diagnosing and treating diseases.[71]

The working principle of silicon nanobelt-base sensors is the field-effect transistor (FET) in which the conductivities of silicon nanowire will be monitored corresponding to the variation of the electric field or potential at the surface of the device. The silicon-nanowire sensors modified with the specific receptor can be used to detect cancer marker protein and single viruses.[71] The capabilities of nanowire / neuron device have many advantages over microfabricated electrodes and planar FET. The advantages included the differences of array geometry and addressable separations, association of n- and p- type elements in well-defined positions, differences in the spatial and number location for the hybrid nanowire / neuron injections, the smaller active junction area (~20 nm wide), simulation of action potential spikes in the soma, and highly integrated system for investigation of synaptic processing in neural networks. The silicon nanowire-based devices represented the specific advantages which related to the structure, size, and

electronic properties of the silicon nanowires. These properties are the key elements for applying to detection of a broad range of medicine and life sciences. However, the Si-nanowire based FET sensors are costly to make and demand special training for users.

The intrinsic chemical and physical properties of carbon nanotubes can offer the unique opportunities to modify the surface of the carbon nanotures. The modified carbon nanotubes may be used as gas sensors[72,73,74] and biosensors[75,76,77,] depending on the surface coverage of analytes. For instance, the carbon nanotubes assembled a network or mesh on the interdigitated electrodes (IDE) surface using a solution casting process which provided the condensed nanotubes performance for gas sensing. The gas-sensing has achieved by monitoring the change of the electrical resistance. The good accessibility for adsorption of gas vapor onto single wall carbon nanotubes (SWNTs) had also been fulfilled at the same time. Based on the theoretical calculation and experiment results, the resistances had been changed due to the mobile number of charge carries that came from charge transfer between absorbed molecules and the SWNT valence band.

The functionalized SWNT can afford biosensing applications. For example, the single-walled carbon nanotube-field effect transistors (SWNT–FET) detected the conductance changes for the processes of specific proteins bonding in aqueous solutions. The proteins (e.g. biotin, staphylococcal protein, (SpA), and UIA antigen) conjugated to the SWNT selectively bound to the target proteins among the other proteins in the solution though the direct electrical conductance

without the labeling. This capability offers opportunities for clinic applications and fabrication of high-density nanotube device. By increasing the contact area of the devices, the detected concentration of specific bonding of protein was reached at 1 pM.[77]

The optical properties (e.g. Roman scattering and photoluminescence) of carbon nanotubes may be not only applicable to the imaging applications,[78,79] but also providing a powerful tool to selectively and sensitively detect proteins.[80] The unique optical properties of SWCNT are high Roman scattering cross-section based on resonance enhancement at near-IR absorption transitions and extremely photostable fluorescence. These properties offer easy and unmistakable detection, no blink, and no diminishment during the period of experiment, with one problem that the detection may not be that portable in field detections.

2.2 Biosensors based on TiO_2-Based Nanostructures

TiO_2 based chemical and biochemical sensors are one branch of the sensors' family of nanostructured materials. Like quantum dots, carbon nanotube, and silicon nanowire, TiO_2 based nanostructured materials such as nanoparticles,[81] nanotubes,[82,83] nanofibers[84,85] and nanpsheets[86,87] have been explored the novel applications for sensing. The gas sensors using flame-made TiO_2 anatase nanoparticles were also developed which can be used to analyze the volatile organic compound and CO at 500 ºC.[88]

Nanoparticles of TiO_2, sized around 45 Å, can be combined with oligonucleotide DNA to form the nanocomposites via covalent bonding.[81]These

nanocomposites presented both TiO_2 nanoparticles property (e.g., intrinsic photocatalytic capacity) and DNA bioactivity. The nanocomposites as the vehicles can be introduced into mammalian cells *in vitro* for initiate intracellular processes and biochemical reactions to express biochemical properties. This method provides a new possibility for medical biotechnology as well as chemistry and material sciences. The exciting and unique property of light-inducible nucleic acid endonuclease is also possessed by the TiO_2-oligonucleotide nanocomposites. The great potential for this technique could become a powerful tool for gene therapy.

The lactate biosensor was illustrated by using hydrogen titanate nanotubes as a promoter for electron transfer.[82] The hydrogen titanate nanotubes not only offered the 3-D porous network for immobilizing lactate oxidase (LOx) as a promoter, but also retained the substrate-specific catalytic activity of enzyme. The advantages of lactate biosensor are lowered the redox potential, removed the oxygen influence from the signal, improved response for lactate acid, and increased the sensitivity.

The titanate nanotubes modified electrodes were used to selectively detecting dopamine (DA) in the presence of ascorbate acid (AA), uric acid (UA), heme protein, and nitrate.[83] The experiments demonstrated the titanate nanotube modified glassy carbon electrode may distinctively separate redox potential for DA from the large excess of AA and UA in pH buffer 7.4. The possible reason was due to the electrostatic reaction between titanate nanotubes and DA, AA and UA. The negatively charged surface of titanate nanotubes would favor positive

cation DA and attracted DA to its surface. On the other hand, the AA and UA would be absorbed by interaction with hydrophilic oxygen-rich groups and caused the electron repulsion, AA and UA rejected for the nanotubes' surface.

The interactions between protein and membrane were studied by using electrochemistry of heme protein, myoglobin (Mb), immobilized on the hydrogen titanate nanotubes. The experimental results illustrated that the protein Mb was not denatured after immobilization on the titanate nanotube modified pyrolytic graphite electrode (PGE) and observed the direct electron transfer from heme center to the electrode. The enzymatic activity of Mb was analyzed by using same electrode in the presence of H_2O_2. The result suggested the excellent catalytic performance such as the lower detection limit and wider liner range.

To monitor nitrate in the water, the titanate nanotube modified electrode were developed to measure 8 mM nitrate in 0.1 M acetate buffer solution. The modified electrode can perform many cycles as switch with on/off function in the acetate buffer solution with and without detected nitrate. This phenomenon offered the potential application for novel nitrate sensors.

The TiO_2 nanofiber doped with LiCl prepared though electrospun was used to detect the humidity.[84] The sensitivity and stability of as-prepared humidity nanosensors improved dramatically compared with that of previous reported in the literatures. The humidity nanosensors explored excellent sensing characteristics such as ultrafast response time ($\leq$ 3s), recovery time ($\leq$ 7s), good reproducibility, and linearity. The oxygen gas sensor based on titanate Nanobelts

synthesized using hydrothermal method exhibited the linear responses for resistance and improved the sensitivity.[85]

The heme proteins, myoglobin and horseradish, may intercalate with titanate nanosheets and maintain in the interlayers of titanate nanosheets.[86, 87] The titanate nanosheets was prepared by solid-state reaction that heated Cs_2CO_3 and TiO_2 at 1027K and exchanged cation to produce $HxTi_2\text{-}x/_4O_4 \bullet H_2O$. The UV-vis experiment demonstrated the good biocompatibility of titanate nanosheets immobilized heme proteins. The heme proteins immobilized on the titanate nanosheet exhibited the fast electron transfer and the good enzymatic activity for H_2O_2 with high sensitivity. The wide linear range and low detection also achieved at same time.

TiO_2 based titanate nanotube is an n-type semiconductor. The biosensors based on the titanate nanotube, like biosensors based on the semiconductor silicon nanowires, have great potentials in developing the nanofibrous electronic devices for direct and label-free detection and sensing that are attractive for medicine and life sciences. Comparing with the synthesized silicon nanowires, the hydrothermal synthesis of the titanate nanofibers is simple, cheap, reproducible, and sensitive to cations present in the system. Thus, a systemically study on the structure of titanate nanofiber would help to well understand interfacial chemical and physical properties and in turn to fully control the electric and optical features.

Chapter 3.

Motivation

3.1 Underexploited Issues Regarding the Titanate Nanofibers:

It was believed that we could use cation exchangeability to study cation intercalated layered titanate nanobelt and electrochemical effect of protein cyt.c on modified electrodes using cation exchanged titanate nanobelts. The layered structure of titanate nanobelts could be characterized using selected area electron diffraction (SAED), high resolution transmission electron microscopy (HRTEM) and X-ray diffraction (XRD). The XRD patterns could show that different cations (H^+, Li^+, Na^+) occupied the interlay space inside the nanobelt and exhibited the various distance between the layers. Thermalgravimetric analysis (TGA) and pH titration may help us reveal the stabilities of structures and surface properties of cation exchanged titanate nanobelts. The measurements of ionic conductivities may show the various surface properties of cation exchanged titanate nanobelts. The electrochemical method could demonstrate that the redox reaction of cyt.c on the modified electrodes using different cation exchanged titanate nanobelts could result in more negative formal potential as cation sizes increase. Presumably, the formal potential of cyt.c might be in the order E°(Na–nanobelt membrane) > E° (Li–nanobelt membrane) > E° (H–nanobelt membrane). Such results may represent that the proton exchanged titanate nanobelts could be more sensitive for redox reaction of protein cyt.c.

3.2. New Basic and Applied Interfacial Nanochemistry to Be Expected:

The cyt.c sits in the inter-membrane space of mitochondria, behaving as an electron carrier in the electron transport chain, thus being redox active and in turn ideal for electrochemical study.[89] Therefore, simply, quickly, and sensitively detecting cyt.c is important. In order to develop multiplexed electrochemical biosensor on bioscaffold, it is crucial to prove a quick electron transfer across the nanobelt-membrane between the redox protein and the solid electrode surface, which defines the need of this work to precisely nanoengineer and chemically modify the nanobelt-membrane on the electrode surface.

One of applications of titanate nanobelt bioscaffold was the controlled drug release.[90] The released chemical species can be detected by using electrochemical methods if electrons can be transferred between species. Dopamine is one of the neurotransmitters in the mammalian central nervous system and has been studied by using microelectrodes for many years.[91] The detection of dopamine released from the synapses has challenges because of the spatial problem and minimal perturbation. Therefore discoveries of new biomaterials of self-assembling 3D scaffold to support the neuron cells growth and detections of the released dopamine become important. Titanate nanobelt bioscaffolds is one of the promising biological materials to study neurochemistry based on its intrinsic physical and chemical properties. The developments of easy to make, cheaper, and disposable biosensors based on titanate nanobelt bioscaffold for clinic use and commercials available are the tasks for the researchers.

Chapter 4.

Characterization Methods

4.1 Powder X-Ray Diffraction (XRD)[92]:

The applications of XRD are determination of crystalline phases and orientation, illustration of lattice parameters, identification of crystallinity and components of a sample. The advantages of XRD are simplicity of sample preparation, rapidity of measurement, and nondestructive. The unique XRD pattern can be a fingerprint of a pure material.

XRD instrument consists of X-ray tube, substrate and detector. The monochromatic X-ray produced from the X-ray tube strikes the sample. The diffraction follows Bragg' law:

$$2d \sin\theta = n\lambda$$

In the equation of Bragg's law, λ is the wavelength of incident beams; d is the distance of two atomic planes; θ is the angle between incident beam and atomic plane in the 0-180˚ arrangement and n is integer. The angle θ collected from the diffraction pattern is known. The d space can be calculated by using Bragg's law. For identification of unknown sample and phase of known sample, using experimental data compare with standards in Joint Committee on Power Diffraction Standers (JCPDS) or International Center for Diffraction Data (ICDF), the information of sample such as crystallographic data, chemical formula, and chemical name can be found.

4.2. Scanning Electron Microscopy (SEM):

The advantages of SEM over the optical microscope are high magnification (10,000 × plus), three dimensional (3D) image, large depth of field, and higher resolution. SEMs imitated the reflecting light microscopes and provide similar information as the light microscopes. SEM can be used to characterize topography and morphology of materials. The topography presented the relationship between surface features and the properties of materials. The morphology showed the shape and size of the sample and demonstrated the relationship between the structure and properties of materials.

SEM may also afford us to characterize the chemical composition and crystallinity of materials. The SEM equipped with energy dispersive x-ray (EDX) analysis may perform the compositional analysis. It provides the ratio of elements and compounds of materials and the relationship between the composition and properties of the material. For single-crystals, SEM illustrates the arrangement of atoms and degree of order of material crystallinity to certain extent.

SEM has three components: electron optical column, vacuum system, and signal detection & display.[93] The function of electron optical column is to produce electrons from the electron source, to form thin, tight, and coherent electronic beam through magnetic lenses, to control and modify the beam from magnetic coils, and to define the beam and prevent electron spray through apertures, etc. The vacuum system consists of a chamber, vacuum pumps, valves, and gauges. The detection system has the secondary detector, and the EDX

detector. The secondary detector provides 3D image with a large depth of field of the sample.

The electron optical column includes first condenser lens, condenser aperture, second condenser lens, objective aperture, scan coils, and objective lens. The general working principle of SEM is that an electron beam is produced by virtual source under high voltage and vacuum. The electron beam is condensed by first condenser lens to form the beam and limit the amount the current in the beam. The condenser aperture constricts the beam and eliminates some high angle electrons. The beam becomes thin, tight, and coherent as it passes through the second condenser lens. The high-angle electrons in the beam are eliminated further from object aperture. The set of scan coils sweep the beam and dwell it. The objective lens focuses the scanning beam onto the part of sample. The interactions between beam and inside sample[94] occur after the beam strikes the sample. The backscattered electrons, secondary electrons, and x-rays are produced from the sample and collected for detection.

4.3 Transmission Electron Microscopy (TEM):

TEM can provide information such as morphologic, crystallographic, and compositional information for a solid sample as small as in atomic scale. The detections of the atomic arrangement and their degrees of ordering for crystallography of the sample are in a few nanometers in diameter. TEM may offer compositional information since it is usually equipped with the EDX.

The great advantage of TEM over SEM is that the observed crystallographic information can be coupled with the image in atomic scale. TEM consists of the following major parts.[95] The illumination system includes electron gun and condensers. The objective lens belongs to the image system. The projective system has several projector lenses. The apertures influence the formation of images and diffraction patterns.

In experiment, the electron-gun produces a stream of monochromatic electrons. The first condenser lens show the spot size of electron beam. The second condenser lens changes the size of the spot from a wide dispersed spot to a pinpoint beam on the specimen. The condenser aperture restricts the beam and knocks out the high angle electrons. The beam hits the sample and parts of it are transmitted. The first intermediate image and diffraction pattern are simultaneously produced by focusing the transmitted beam through objective lens; the electron diffraction pattern is focused on the back focal plane. The image formed by objective lens is enlarged through the intermediate and projector lenses all the way. The optional objective aperture may enhance the contrast since it blocks the high angle diffracted electrons. The function of selected area aperture enables the user to get diffraction pattern from a specific area.

4.4 High Resolution Transmission Electron Microscopy (HRTEM)[96]:

TEM has three imaging formations. They are mass-thickness contrast, diffraction contrast, and phase contrast. The mechanisms for both mass-thickness and diffraction contrast are based on change amplitude of the electron waves.

However, the phase contrast does not need the objective aperture or use a very large objective aperture to ensure that all the beams (transmitted and diffracted beams) are contributed to form an image. HRTEM can demonstrate the imaging of lattice fringes in which the spacing and interaction angles are same to those of specific planes in the crystal. It helps users to illustrate how the atoms in a specific structure are periodically arranged.

4.5 Thermogravimetric Analysis (TGA)[97]

TGA is an analytic technique that characterizes a material's thermal stability associated to decomposition, dehydration, oxidation or reduction, phase transformation, etc. TGA monitors these properties though the weight loss or gain of the sample as a function of temperature in a controlled atmosphere.

The analyzer of TGA has a high-precision balance and a small pan for loading the sample. The pan is in the electrically heated oven which has a temperature controller. The temperature in the oven routinely reaches 1000℃ or higher. The oven is insulated greatly in order to keep the system away from any change in the environmental temperatures. The inert or desired gas is purged to the oven so as to avoid undesired redox reactions or other chemical and physical changes during the testing. The weight, temperature, and temperature changes are measured in TGA measurements with a high degree of precision. The weight loss curve represents the relationship between the weight loss and the heated temperature; however the derivative curve of the weight loss provides the points at which the more accurate temperature for weight loss is identified.

4.6 Fourier-Transform Infrared spectroscopy (FTIR):

The wavenumber (cm^{-1}) of mid infrared (IR) spectroscopy in electromagnetic spectrum is from 4000 to 400 cm^{-1}.[98] Usually organic molecules absorb infrared radiation and convert the absorbed energy to the energy of molecular vibration. IR can be served as a fingerprint for chemical components because the absorption occurs just as the radiation energy is matched the energy of the specific molecular radiation.

IR can be used to monitor chemical reactions *in-situ*, identify an unknown compound, determine chemical groups in a specific compound, and characterize optical conductivity. IR method may measure samples, such as solids, liquids, and gases. IR is a quick and cheaper spectroscopic technique comparing with nuclear magnetic resonance spectroscopy (NMR) and mass spectroscopy (MS).

FTIR instrument includes the source, the interferometer, the sample hold, the detector and the computer.[99] The source emits the infrared energy and the beam passes through an aperture that controls the portion of energy transferred to the sample. The function of the interferometer is to convert the beam into the interferogram signal which passes the sample. The beam transmits through or reflects off from the sample surface depending on the type of analysis and measures from the detector. The measured signal transfers to the computer to produce the final infrared spectrum for the sample.

4.7 Electrochemical Methods[100]:

4.7.1 Cyclic Voltammetry (CV).

CV is an important and common analytic method in electrochemistry. CV can be used to find the information about the electroactivity of compounds, to monitor coupled chemical reactions, to determine the mechanisms and rates of oxidation/reduction reactions, to study the electrode surfaces, etc.

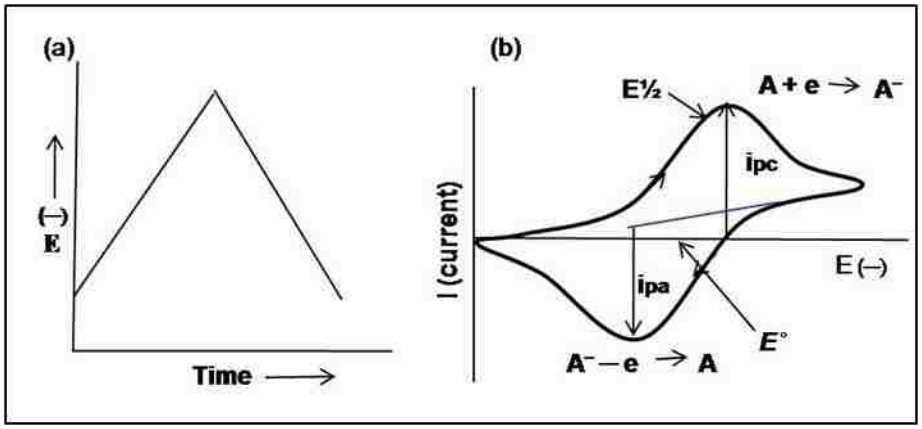

Figure 4.1 (a) The applied the potential (b) the curve of CV[100]

The electrochemical cell for CV usually has three electrodes: working electrodes (WE), counter electrode (CE), and reference electrode (RE). In the CV experiment, the applied potential is needed to desire levels depending on the electroactive species. The potential of WE is linearly changed as the applied potentials sweep back and forth with time, as shown in Figure 4.1(a). The current passes through a WE and a CE in an electrolyte solution, and the current of the working electrode is measured as a function of potential. The potential of the WE is measured with respect to the RE during the potential scan.

As the potential increases during the scan, as shown in Figure 4.1(b), the electroactive specie (A) will gain an electron. In a reduction reaction, the A will be reduced to A^- at the WE, resulting in a cathodic current. As the potential scans to the opposite direction in an oxidation reaction, the A^- will lose an electron and be oxidized to the A at the WE, resulting in an anodic current.

For the electrochemically reversible (Nernstian) redox reaction, the important parameters are peak potential (E_p), half wave potential ($E_{1/2}$), anodic peak potential (E_{pa}), cathodic peak potential (E_{pc}), the difference of the peak potentials (ΔE), and peak currents (i_{pa} and i_{pc}). For the reversible (Nemstian) reaction, the peak potential does not change for the various scan rate and concentrations. The peak separation (ΔE) is 59 / n (mv). I_p depends on the square root of the scan rate. The calculation equations are listed below.

$$E_p = E_{1/2} +/- 1.109\ (RT/nF)$$

$$\Delta E = | E_{pa} - E_{pc} | = 2.3\ (RT/nF) = 59 / n\ (mV)\ (\text{at } 25\ ^oC)$$

$$i_p = k\ n^{(2/3)}\ A\ D^{(1/2)}\ c\ v^{(1/2)}$$

$$E = E^\circ + (RT/nF)\ \ln[Co]/[C_R]$$

where, T: temperature (K)

n: the number of electrons (eq/mol)

F: Faraday's constant (96,485 e/eq)

A: electrode area (cm^2)

D: diffusion constant (cm^2/s)

c: the bulk concentration (mol/cm^3) of the redox species

[Co] ([C_R]): the concentration of oxidized (reduced) specie at the electrode surface

E°: the formal electrode potential of redox specie

E: the applied potential

v: scan rate (V/s)

k: Randles-Ševcik-constant ($2.69*10^5$ $A.s.V^{-1/2}$ mol^{-1} at 25 ˚C)

4.7.2 Differential Pulse Voltammetry (DPV).

Pulse methods included DPV and Square Wave Voltammetry (SWV) have many advantages over cyclic voltammetry such as minimizing background charging current and enhancing sensitivity and speed. For DPV, the potential wave form applied to the working electrode is a sequence of pulse showed in Figure 4.2(a). The pulse period, pulse width, pulse amplitude, step E, and sample period are parameters of the DPV. The current is measured at the points of the beginning and end of the each pulse period. The selected sampling points are allowed for the decay of nonfaradaic current. The resulting differential pulse voltammogram is presented in Figure 4.2b.

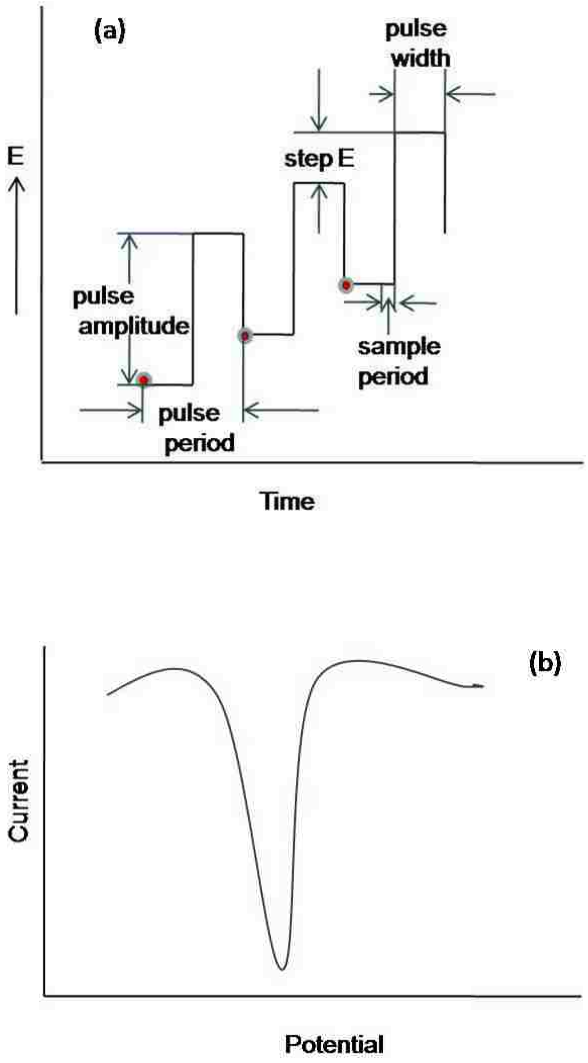

Figure 4.2 (a) The applied the potential wave form

(b) The resulting differential pulse voltammogram[100]

4.7.3 Square Wave Voltammetry (SWV).

The advantages of SWV are high sensitivity, rejection of background current, high signal to noise ratio, and lower detection limit (as low as 10^{-8} M).

The applied excitation signal in SWV is a symmetrical square-wave pulse showed in Figure 4.3(a). The amplitude (ΔE_p) is superimposed on a staircase waveform of step height ΔEs. The t_p is a pulse width. The net current is produced by taking the difference between the forward (i_2 at point 2) and reversed current (i_1 at point 1). The peak height (i_p) showed in Figure 4.3(b) is increased as the concentration of the redox species increases.

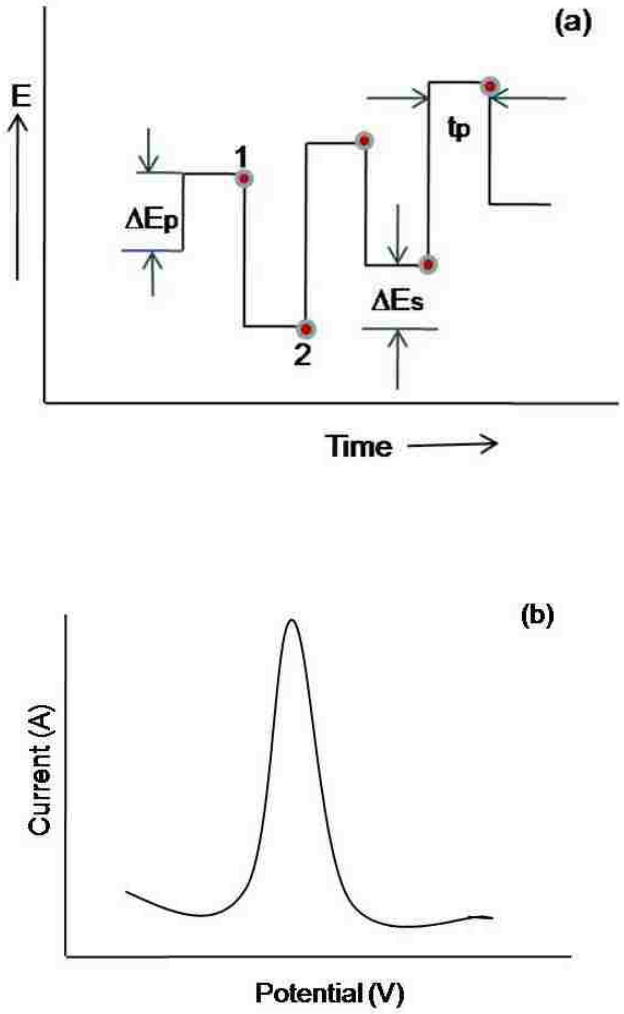

Figure 4.3 (a) The applied potential wave form

(b) The resulting square wave pulse[100]

Part II. EXPERIMENTAL

Chapter 5.

Materials and Instrumentations

5.1. Chemicals.

Horse-heart cytochrome c (cyt c) was purchased from Sigma, and used without further purification. Dopamine and ascorbic acid were purchased from Sigma and used without further purification. NaOH, KOH, K_2HPO_4, KH_2PO_4, and H_3PO_4 were of analytic grade, purchased from VWR. TiO_2 powder (Degussa P25) was used as received.

Three phosphate buffer solutions were prepared from K_2HPO_4 and KH_2PO_4. The pH values adjusted using KOH and H_3PO_4 were prepared to 5.5, 6.8, and 9.0 in distilled deionized water (DDI water, pH ~ 6.5), respectively. The concentrations of buffers were 0.04 M.

5.2. Instrumentations

The XRD is a Rigaku Miniflex X-ray diffractometer using as radiation source the Cu Kα (λ = 1.5405Å). The range of 2θ was 5 -15° with a 0.02° step and a step time 1.25 s.

XRD sample preparation was done typically by dropping the sample on the surface of the silicon wafer (111) or a glass micro slide to make an area of sample in 1 cm×1 cm and then drying the sample at room temperature.

The size and morphology of titanate-nanobelts were analyzed by using SEM (Philips ESEM XL30) and TEM (JEOL X-100). The structure of layered titanate nanobelts was characterized by using HRTEM (Titan 80-300S).

SEM sample preparation was done typically by taking a piece of carbon conductive tape and putting it on a clean specimen stub first. Then, the sample was dropped on the surface of carbon conductive tape and dried in air at room temperature, and finally coated with Ag in a sputtering coater. HRTEM sample, however, was prepared by dropping the samples on the surface of the TEM holder and then drying the sample at room temperature.

TGA study was carried out using STA 409 PC LuXX® . The temperature range was from room temperature to 500 ˚C with a heating rate of 10 K/min. under a nitrogen gas flow. The sample weight is around 5-10 mg. The Fourier transform infrared spectroscope (FTIR) was a Bruker TENSOR 27 Spectrometer at the resolution of 2 cm^{-1} in wavenumber.

Electrochemical workstation (model 660B, CHI-instrument) was used for electrochemical sensing measurement. The pH meter (METTLER TOLEDO) was used for measuring the pH values of solutions.

Chapter 6.

Preparations and Characterizations of H–Titanate Nanobelts

6.1 Syntheses

TiO_2 (0.020 g) was added in an aqueous NaOH or KOH solution (10 M, 10 ml). The mixture was then put into a Teflon-lined stainless steel autoclave container and heated at 180 – 240 °C for 3-10 days. The resultant white pulp-like suspension was washed with the distilled water until the solution reaching pH 7. The product was then air-dried at room temperature (RT).

6.2 Ion-exchange

Ion exchange solutions were prepared by dissolving LiCl, NaCl, and HCl in DDI water to make 1 M concentration. The as-prepared titanate nanobelts were put in the solutions (1 M) of HCl, LiCl and NaCl and stirred them at room temperature (RT) for several days, respectively. The products were thereafter washed with DDI water to remove the salts or dilute HCl until no pink color on the pH paper (pHydrion^{TM} MIKRO 1-12).

6.3 Preparation of Cyt c and Dopamine Solutions.

Two stock solutions of cyt c were prepared by dissolving 2.0 mg and 3.7 mg of the protein in 1 ml of the pH 6.8 phosphate buffer solutions, respectively.

Dopamine solutions in DDI water were likewise prepared freshly before test. The concentration were 0.21 mM, 0.11 mM, and 42.2 μM.

6.4 Fabrication and Characterization of the Nanobelt-Membrane Modified Electrodes (ITO, Glassy Carbon)

6.4.1 Preparation of ITO Electrodes That Are Modified by Nanobelt-Membrane and then Immobilized by Cyt c

ITO (fluorine doped tin oxide) glasses (with the resistance of 13 Ω /mm^2) obtained from Hartford Glass Co., Inc., each about 2.5 cm × 0.8 cm in size, were cleaned by sonication for 5 minutes in 15 ml of acetone, then 15 ml methanol, 15 ml isopropanol, and 15 ml DDW, respectively.

The titanate-nanobelts were introduced onto the ITO surface, and dried at RT in air overnight. Afterwards, the cyt c solutions, 15 μl ranging from 3 (μM) to 30 (μM) in concentration (or about 45 to 450 picomoles), were added onto the titanate-nanobelt surface and dried at the RT before use.

6.4.2 *Preparation of Glassy-Carbon Electrodes That Are Modified by Nanobelt-Membrane and Immobilized by DA*

Glassy carbon (GC) electrodes from CHI-instrument (Austin) were cleaned by sonication for 5 minutes in 15 ml of acetone, then 15 ml methanol, 15 ml isopropanol, and 15 ml DDI water, respectively. After every experiment, the

GC electrodes were polished with alumina slurry 1.0 μm, 0.3 μm, and 0.05 μm, respectively on polishing cloth with DDI water and then cleaned using DDI water.

The titanate-nanobelts were evenly applied onto the GC surface, and dried at RT in air overnight. Afterwards, a solution of 15 μl DA was added onto the titanate-nanobelt surface and dried at the RT before use.

Chapter 7.

Interfacial Characterizations of Nanobelt-Membranes

7.1 Ionic Conductions

This work was performed using a PTFE cell (1 ml volume) pre-filled with deionized water (pH adjusted to 7 using KOH). The active electrode containing the membrane was connected to the head-stage of an Axopatch 200B instrument (working in Voltage Clamp mode), feeding a “Digidata 1440” digitizer (Molecular Devices). The second electrode (ground) was an Ag/AgCl wire. Both electrodes were embedded into the working solution, which was continuously stirred by a low noise Spin-2 Stir Plate (Warner Instruments). The current traces were recorded and analyzed using the Clamp fit 10 software package (Molecular Devices). Small aliquots of stock solutions (HCl 1mM-10mM, and NaCl 2M) were added to the cell in order to change the ionic strength or pH.

7.2 Biocompatibility to Cytochrome c

FTIR was used to examine the biocompatibility of cyt c immobilized on the sample. The nanobelt-membrane, pre-immobilized with cyt c, was mixed with KBr powder in a die and pressed into pellets for FTIR measurements.

7.3 Point of Zero Charge (PZC) on H–Titanate Nanobelts Membranes

To estimate the PZC on membranes of intercalated titanate nanobelts, firstly pH Solutions from 2-12 were prepared by using 01 M HCl and 0.1 M NaOH. The pH values of solutions were measured by standard pH meter. Secondly, put the dried samples of intercalated titanate nanobelts into the pH solutions (pH values: 2 – 12) to make the suspension. The ratio of the dried sample to pH solution was 0.4 mg/ml.[101] The suspensions would be rotated overnight at room temperature. The purpose of rotation was to make the surface of nanobelts to have enough time to expose to the pH solution. The clear solution would be obtained after centrifuging rotated suspension. The final pH value of each suspension had been measured from the clear solution.

Chapter 8.

Neuron-regenerations and Biosensing on H–Titanate Nanobelts Membranes

8.1 Pheochromocytoma (PC-12) Cell Culture.

Membranes of titanate nanobelt-scaffolds were first sterilized in 70% ethanol, and then put into culture plates. PC-12s (1 million cells/ml)[102] (from American Type Tissue Culture (http://www.atcc.org) were grown on the membranes in the RPMI-1640 media that was supplemented with 1% penicillin/streptomycin, 10% horse serum (both heat inactivated), and 5% fetal bovine serum in the humidified atmosphere with 5% CO_2 at 37°C. The cells had been cultured for 72h on the rat-tail collagen-coated plates by plating at densities (1 million cells/ml) to produce 80% confluence on the titanate membranes before they were used for exposure studies.

8.2 Electrochemical Sensing of Cytochrome c

A three-electrode system was used in the electrochemical measurement. The working electrode (WC) was the ITO glass modified by the titanate nanobelts with or without the cyt c immobilization. The electrochemical sensing was performed at the room temperature (RT) on an Electrochemical Workstation (660B, CHI-instrument), with a platinum counter electrode (CE) and an Ag/AgCl

(3.0M KCl) reference electrode (RE). The buffer solution was purged with ultrahigh purity nitrogen gas (from AirGas) at least 10 min. prior the sensing tests. A nitrogen environment in the electrochemical cell was maintained throughout each of the sensing tests.

8.3 Electrochemical Sensing of Dopamine

A three-electrode electrochemical cell was used in the CV and DPV tests. The cell consisted of the working electrode that was the glassy carbon coated with the titanate-nanobelt, a platinum counter electrode (CE), and an Ag/AgCl (3.0M KCl) reference electrode (RE). The electrochemical sensing was performed at the RT using the electrochemical workstation (660B, CHI-instrument). The buffer solutions were purged with ultrahigh purity nitrogen gas (AirGas) at least 10 minutes before the sensing test. A nitrogen protection environment in the electrochemical cell was maintained throughout each of the sensing tests.

PART III RESULTS AND DISCUSSIONS

Chapter 9.

Structures and Surfaces of Intercalated Titanate Nanobelts

9.1 Crystal-Lattices of the Intercalated Titanate Nanobelts

Titanate nanobelts had been synthesized by hydrothermal method in autoclave. The reactants included 10 M NaOH and TiO2 (P25) in autoclave were in the liquid phase during the hydrothermal reaction. The synthesized temperature (~200 ˚C) was lower the critical temperature (~396.4 ˚C) of NaOH (25 %, wt).[103] The higher concentration of NaOH has a higher critical temperature. The reaction temperature and local concentration of Ti (IV) in the autoclave are the most important parameters that affect the formation of nanofibers instead of nanotubes. Titanate nanofibers was formed mainly through two steps.[104] First of all, raw TiO_2 had been accompanied to titanate nanosheets by the epitaxial grown at temperature around 200˚C. Secondary, the higher concentration of Ti (IV) may increase the rate of nanosheets growth. The rate of crystallization was high enough which made the titanate nanosheets became thicker and rigid, and then the nanosheets formed nanofibers.

The schematic illustration below clearly depicts a titanate nanobelt's layered lattice structure that is surfaced alternatingly by negative-charged framework layers $(Ti_3O_7)^{2-}$ and interlayer counter-cations. The octahedrons of

[TiO_6] are corner- and edge-sharing in the framework [see ORTEP (Oak Ridge Thermal Ellipsoid Plot) illustration]. Topologically, the cation population on the nanobelt surface is less than that inside the interlayer space. The as-made titanate nanobelts may have some protons and distributed in the interlayer.[105]

To understand roles of the interlayer-cations at the nanobelt-water interface, intercalations of H^+, Li^+, and Na^+ were conducted first of all at room temperature (RT) in 1 M HCl, LiCl, and NaCl solutions, respectively. X-ray diffraction (XRD) data (Fig. 9.1a) confirm that the (002) diffraction-peak appears at 2θ= 11.14° (d = 0.79 nm) for H^+-intercalated nanobelt membrane (nanobelt mambrane), 10.69° (d = 0.826 nm) for Li^+- intercalated nanobelt membrane, 9.81° (d = 0.901 nm) for Na^+-nanobelt membrane, respectively. The cation exchanged nanobelts kept the same morphology showed in Fig.9.1b. The $d_{(002)}$ of 0.79 nm is supported by the lattice-fringe image from a high resolution TEM (HRTEM) study (Fig. 9.2).

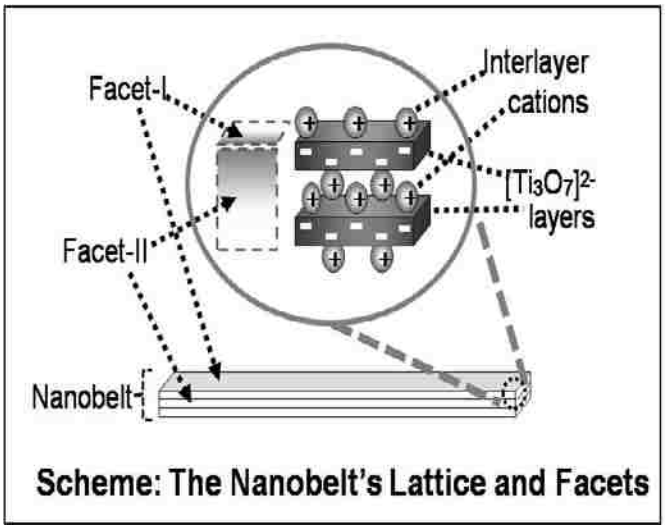

Scheme: The Nanobelt's Lattice and Facets

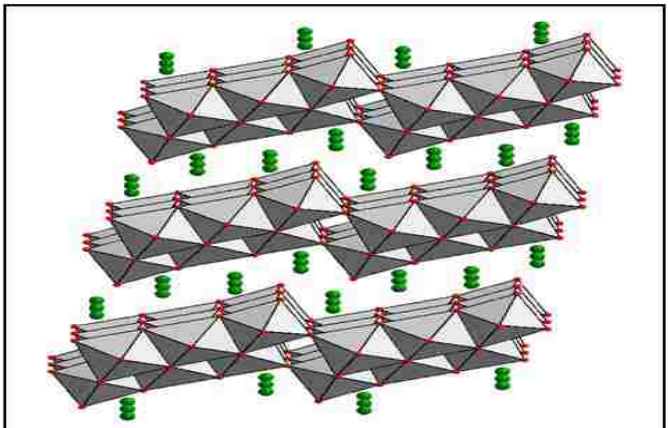

ORTEP illustration for titanate crystal structure

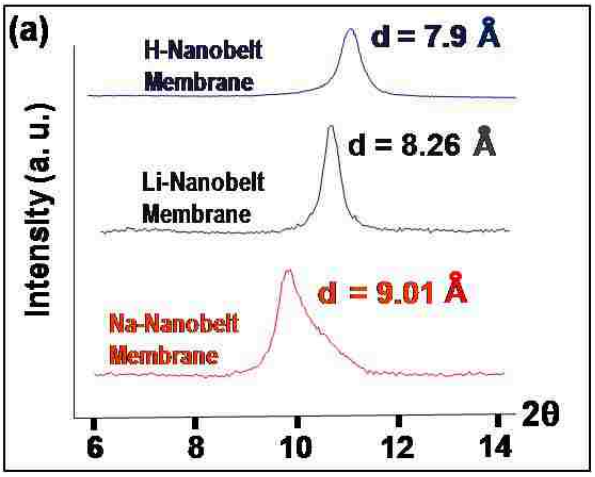

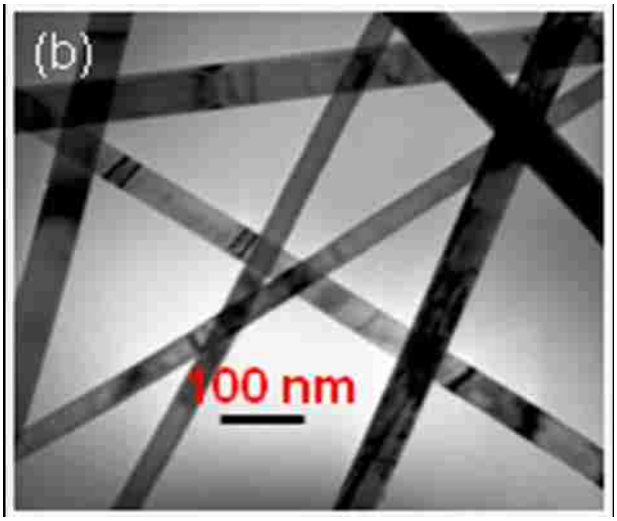

Figure 9.1 (a) XRD patterns of titanate nanobelts: Blue color is for H^+–, gray for Li^+–, and red for Na^+–nanobelt membranes. (b) H^+–nanobelt TEM image

The increase in the d-space $d_{Na\text{-nanobelt membrane)}} > d_{(Li\text{-nanobelt membrane)}} > d_{H\text{-nanobelt membrane)}}$ is in line with that for anhydrous cation-radii {Na^+ (~0.096 nm) > Li^+ (~0.060 nm)}, but contrary to that for hydrated cation-radii {$Li^+_{(aq.)}$ (0.34 nm) > $Na^+_{(aq.)}$ (0.28 nm)}[106] . Therefore, the interlayer-space should be occupied by minimally hydrated counter-cations, and the ion-exchange process should be accompanied by a dehydration of hydrated cations, which is unusual because in other layered transition metal oxides the interlayer cations are often highly hydrated[107]

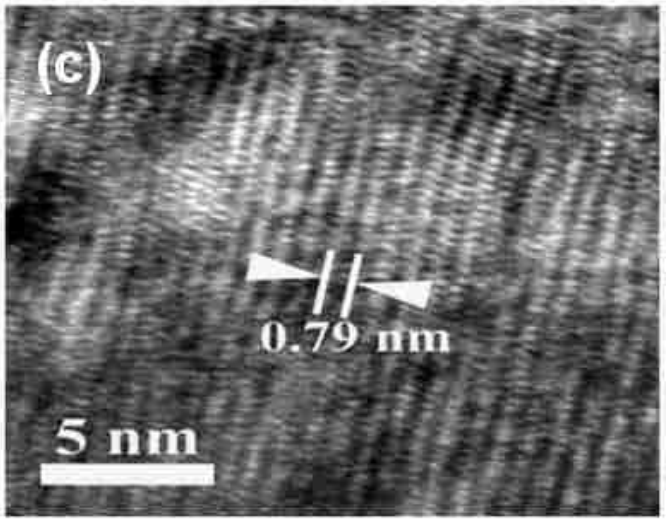

Figure 9.2 HRTEM lattice-fringe image for a H^+–nanobelt.

A minor peak of H-intercalated lattice did sometime appear in the XRD patterns of both Li^+- and Na^+-intercalated nanobelt membrane if the ion-exchange was not well controlled. This tells that the H^+ (~10^{-6}–10^{-7} M) in aqueous solutions of LiCl (~1.0 M) and NaCl (~1.0 M) can compete with millions of times more Li^+ and Na^+ in the intercalations within the same time-

period, due likely to the smaller diameter and thus higher diffusion-rate and mobility of the H^+. In contrast to much larger Li^+ and Na^+, the H^+ may easily reach the charge-balancing sites throughout the lattice, and introduce the least structural distortion and inter-cation repulsion in the interlayer space, both probably favorable in kinetics and thermodynamics. The researchers illustrated[108] that the protons in the interlayer have two different binding energies since the oxygen atoms are located different. Very small amount of the protons which are located near the center of nanobelts and have higher binding energies may not show cation intercalation and kept in the interlayer. Very likely, the H^+ could be even mix-intercalated with Li^+ or Na^+ in the lattices thus further reducing the intensities of the XRD-peaks and broadening the peaks in XRD pattern. The broaden peaks in the XRD pattern can be caused by other reasons such as the crystallite size, microstrain, and solid solution inhomogeneity.[109] The exchanging H^+ with large Li^+ and Na^+ may not be as easy as doing the opposite. During the intercalation, the diffusion of the cations on the nanobelt surface is faster than that in the interlayer.

The titanate nanobelts possess an entangled morphology that is full of micropores, mesopores, and macropores. SEM image (Fig. 9.3a) shows a cross section of H-titanate nanobelt membrane on an ITO-substrate. The two small arrows indicate a single nanobelt in the membrane. Figure 9.3b shows an SEM image of as-made titanate nanobelts from hydrothermal syntheses.[110]

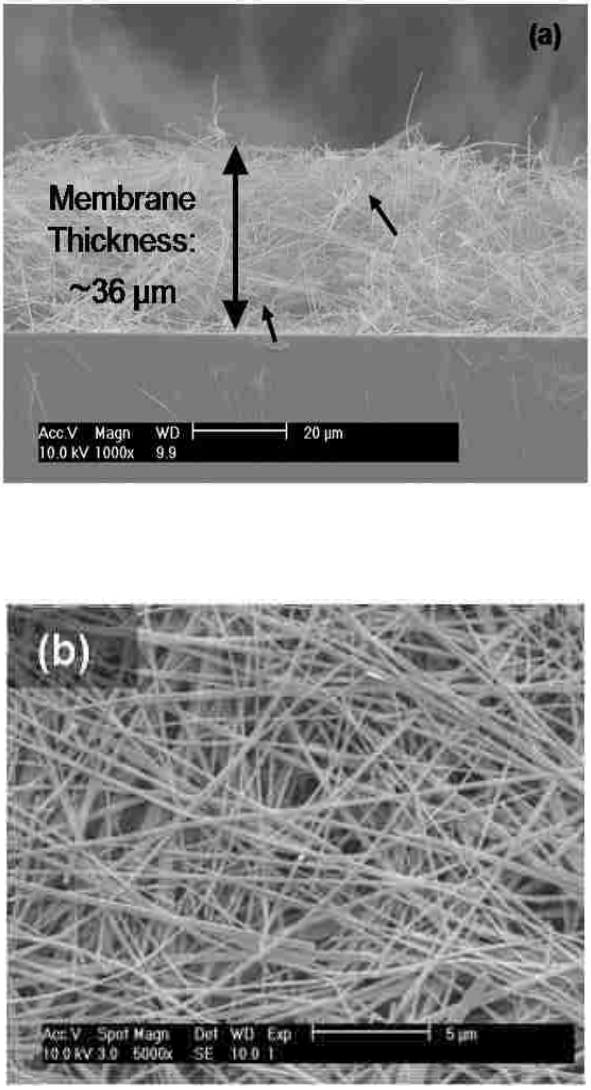

Figure 9.3 Nanobelt Characterizations. (a). A cross-section SEM image of a 36-µm-thick H-nanobelt membrane on an indium-tin-oxide (ITO) substrate. (b) An SEM image of titanate nanobelts synthesized from hydrothermal method.

9.2 Thermal Stability of Intercalated Nanobelt

The thermal stability of cation exchanged titanate nanobelts reflects the hydration difference in the structure for the various cations in titanate nanobelts. Figure 9.4 shows the thermogravimetric analysis (TGA) for Na^+–exchanged nanobelts and H^+–exchanged nanobelts from room temperature to 500 ˚C. One of the endothermic peaks from derivative of mass loss at temperature 115 ˚C for Na^+–exchanged nanobelts (lower part in Fig. 9.4) demonstrates the mass loss that is due to the physically absorbed water on the titanate-nanobelt surface. The other endothermic peaks at 132 ˚C for H^+–exchanged nanobelts (upper part in Fig. 9.4) and 178 ˚C for Na^+–exchanged nanobelts (lower part in Fig. 9.4) represent loss of the interlayer water that intercalated between crystal layers in the titanate structure.[111,112,113] The TGA plot represents the fact that 2 H_2O lost from every H^+–exchanged titanate, and 1.5 H_2O from Na^+–exchanged titanate due to more protons were in the crystal lattice for H^+–exchanged nanobelts and easily diffused out from the crystal lattice.[114] As the temperature is higher than 300˚C, no peaks are observed from both of H^+–exchanged nanobelts and Na^+–exchanged nanobelts. The cation–exchanged nanobelt continually dehydrated until the temperature reached 500 ˚C that implied the structures of cation exchanged nanobelts are stable. The water losses from the titanate structure needed higher temperature.[115]

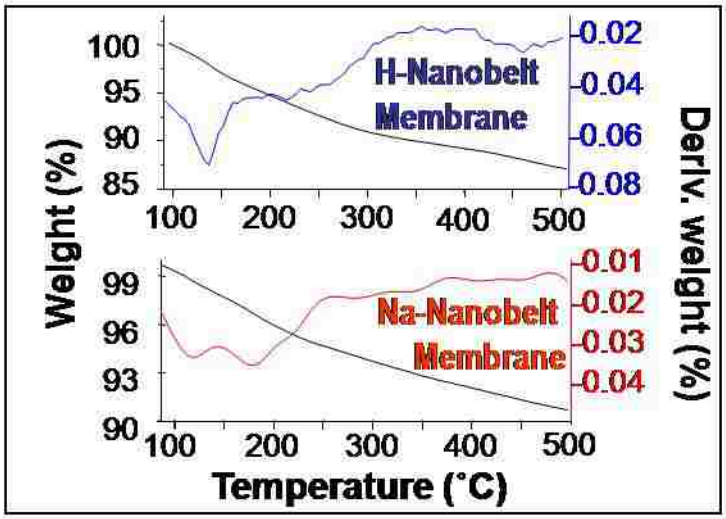

Figure 9.4 TGA analysis for H^+–exchanged (upper) and Na^+–exchanged (lower) nanobelt-membranes obtained at 10 K/min under flowing N_2 from room temperature to 500˚C ; Black color is for weight loss (%), blue or red for derivative of the weight loss (%).

9.3 Surface of Intercalated Nanobelts

To determine the difference of one of the surface properties of the cation exchanged titanate nanobelt, i.e., point of zero change (PZC), simple titrations may offer some useful information for the surface property via monitoring the proton concentration. The final pH values of solutions represented the equilibrium of the proton concentrations between surfaces $[H^+_s]$ for cation exchanged titanate nanobelt with $[H^+]$ in the bulk solutions[116], also it reflects the point of zero charge (PZC)[117] of cation exchanged titanate nanobelts. The relationship of proton concentrations on the immersed solid surface to the bulk solution is represented[116]

$$[H^+_s] = [H^+] \exp(-y_0) \qquad y_o = e\psi_0/kT \qquad (1)$$

From equation 1, the surface potentials are different for the cation exchanged titanate nanobelts since cations are different in the interlay[108] The Na^+ cations are weakly bounded to the $[TiO_6]$ octahedra comparing with protons. The electronic and geometric $[TiO_6]$ octahedral were redistributed after cations intercalation and then the surface potentials were changed respectively. The difference on surface potentials for cation exchanged nanobelts is unclear. The $[H^+_s]$ on the surface of H^+— exchanged titanate nanobelt expected higher than that of Na^+— exchanged titanate nanobelt since H^+— exchanged titanate nanobelt was formed in acidic solution in which the H^+ cations in the solution replaced the Na^+ cations in the interlayer of titanate structure. The TGA data and XRD patterns have also been proved this fact. The ratio (Z/r) of cationic charge (Z) to its radii (r) is the other parameter that affects the PZC of solid oxides. For the same

charged cations in the interlay, the ratio decrease as the cation size increase, the PZC would be shifted to the higher value (or increase PZC).[118]

In the crystal structure of nanobelts, the –OH groups (Lewis base) on the facets may interact with nearby counter-cations (Lewis acid) to influence the acidity/basicity at the nanobelt-water interface. These may also affect surface properties such as point of zero charge (PZC). Figure 9.5 displays two curves, each with a plateau for estimating the PZC. The Na^+-intercalated nanobelt membrane showing a PZC ~9.8 (the red plateau) can behave as a membrane-buffer near pH 9.8, while the H^+-intercalated nanobelt membrane's surface with a PZC ~ 4.1 (the blue curve) can act as a membrane-buffer near pH 4.1. This phenomenon suggests (i) a continuous $H^+ \Leftrightarrow Na^+$ ion-exchange may enable the nanobelt membrane to buffer within pH 4–10 at the nanobelt membrane-water interface and (ii) the capacity and kinetics of the nanobuffering may reflect that of the intercalation of the nanobelts. Since H^+ is a strong Lewis-acid guest while Na^+ a weak Lewis-acid guest, the sheet-framework $(Ti_3O_7)^{-2}$ ought to be a medium Lewis-base host, based on the "conjugated acid-base" chemistry. This phenomenon also implied the difference of the one of the surface properties for Na^+— exchanged titnante nanobelt and H^+— exchanged titanate nanobelt such as PZCs.

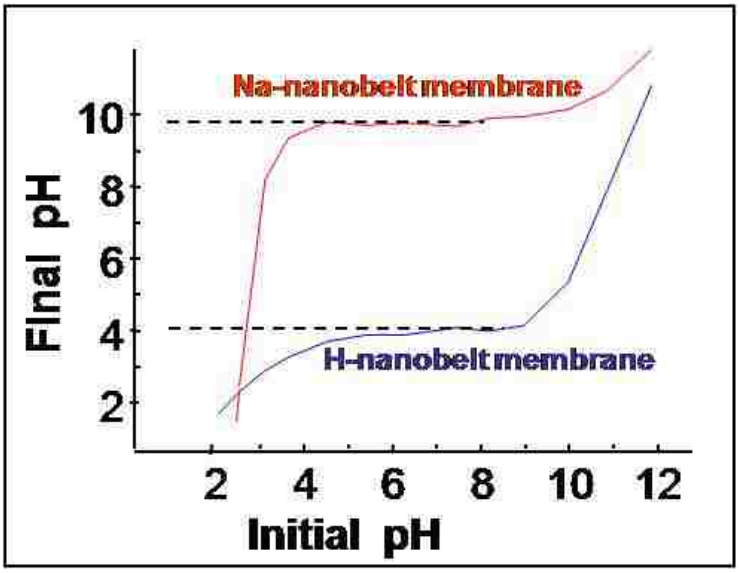

Figure 9.5 The measurement of pH change for cation exchanged titanate nanobelts in various pH solutions/suspensions; red: Na^+– exchanged titanate nanobelt; blue: H^+– exchanged titanate nanobelt.

9.4 Ionic Conductivity of Intercalated Nanobelts.

The conduction of H^+ and Na^+ across both the H^+- and Na^+-intercalated nanobelt membranes were evaluated. At 0.5 mM of cation concentration (the dotted line in Figure 9.6), the current of H^+ across the H-nanobelt membrane (black) is ~50 (nA), while that of H^+ across Na-nanobelt membrane (blue) ~4.5 (nA), that of Na^+ across Na-nanobelt membrane (red) ~3.5 (nA), and that of Na^+ across H-nanobelt membrane (green) ~2.0 (nA), respectively. Since the membranes were similar in size, the density of H-current (black) is >10 times higher than that of any other three, compared our results with the recent published paper for proton transport in aligned mesoporous silica films,[119] The higher currents of transported Na^+ cation and proton in the exchanged membranes of the H-nanobelt membrane and Na-nanobelt membrane, the smaller proton concentration, thinner film, and easier to synthesize and prepare film are achieved.

The mobile and acidic H^+ may have no net-intercalation during the H^+-transfer across the acidic H-nanobelt membrane thus the largest current (the black curve in Fig. 9.6), with a flatter slope at the curve-beginning is due likely to a rapid interaction between the transferring H^+ and the –OH group on the H-nanobelt membrane. The $Na^+ \Leftrightarrow H^+$ ion-exchange and the acid-base "neutralization" can slow down either cation's conduction. The basic Na-nanobelt membrane (PZC~9.8) conducts acidic cations (H^+, Na^+) poorly, which correlates the interfacial acidity/basicity with the ion-transfer at the membrane-water interface as "like conducts like". As a complement to spherical nanoparticles of

layered phosphates[120], charge-transfers along the long nanobelts across the nanobelt membrane involve fewer grain-boundaries thus less energy-loss or nanoscale heating and the corresponding lattice-distortion than that across powder-pressed membranes, which could help develop heat-resistant membrane-electrodes for Li-battery, fuel-cell, solar-cell, etc.

In comparison with the Na-transfer across typical biological cell-membranes which depends on the density of protein-based Na-pumps and channels,[121] the Na-transfer across the Na- and H-nanobelt membranes shows relatively high current-densities. Such thermal-stable ceramic H-nanobelt membrane could be useful in developing heat-resistant proton-exchange membrane fuel-cell (PEMFC) and membrane-like Li-batteries.

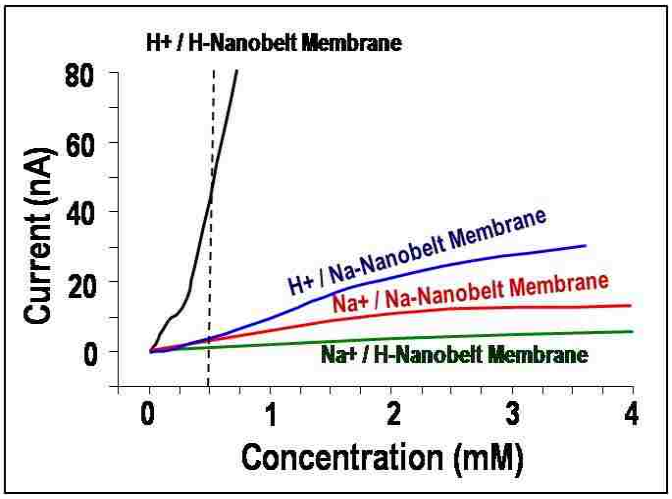

Figure 9.6 Correlations between the ion-concentrations and the ionic currents. The black curve: H^+ across an H-nanobelt membrane, blue for H^+ across a Na-nanobelt membrane, red for Na^+ across a Na-nanobelt membrane, and green for Na^+ across the H-nanobelt membrane.

9.5 Conclusion

Titanate nanobelt, with a layered crystal lattice and a typical diameter of 70-nm and length up to 3 cm, has been proven in this work for the first time to possess underexploited zwitterionic surfaces that are surfaced alternatingly by $(Ti_3O_7)^{2-}$-framework layers and exchangeable interlayer cations. On this basis, we have defined new functions of biocompatibility, ionic conductivity, pH- and electrolyte-buffering on a paper-thin filtering membrane self-entangled by the low-cost nanobelts, which has been seldom demonstrated in literature so far. By tuning the cation-exchange continuously on the zwitterionic surface of the thermally and chemically stable nanobelt-membranes, we have simultaneously conducted proton, and buffered pH and electrolytes in water, which is unfeasible on DNA-, protein- and polymer-based bioscaffolds. As a first attempt to exemplify rich chemistry at the nanofiber-water interface in a confined 1D environment, this work is believed to be generally applicable to 1D nanomaterials with the layered and even porous crystal-lattices in both membrane- and separate fiber-forms.

Chapter 10.

Biosensory Membrane-bioscaffolds of H-Titanate Nanobelts

10.1 FT-IR Characterization for Cyt c on the H-Nanobelts

It is known that a protein could be destabilized after binding to the negatively charged surfaces such as lipids.[122, 123, 124] FT-IR is a commonly used technique to study the secondary structure (or folding) of protein's polypeptide backbone. The amide groups of polypeptides are sensitive to the protein conformation, and the amide I (1700-1600 cm^{-1} region) is primarily due to the C═O stretching vibration of protein's backbone. FT-IR spectra (see Fig 10.1a) show a peak at 1648 cm^{-1} for amide I[125] of immobilized cyt c on the nanobelts, which is at the same position as that of native cyt c in buffer solution at pH 6.8, indicating the retained secondary structure for the cyt c immobilized on the titanate-nanobelts. The secondary structure of protein cyt c was also examined in an acidic solution using FT-IR (see Fig 10.1a). There were two separated peaks ranging from 1600-1700 cm^{-1} in acidic solution which are absent in neutral solution (pH=7). The peak at 1648 cm^{-1} present in the neutral solution was found to be significantly reduced in intensity as compared to in the acidic solution. These results suggest the changed secondary structure of cyt c .[126,127] The FT-IR results illustrate that cyt c after immobilization on the titanate nanobelt still exists in the normal condition. However, to confirm the biocompatibility of cyt c immobilized on titanate nanobelt, more evidence is needed by the use of other techniques such as UV-Vis and circular dichroism (CD).

10.2 Neuron Cells Growth on H-Titanate Nanobelt Scaffolds

The scaffolds could facilitate cellular activities. SEM images (Figure 10.1b) showed that the PC-12 cells attached well and formed cell colonies on the titanate-nanobelt bioscaffolds after 72 h, suggesting a good compatibility between the cell and the scaffold. The cells appeared round in shape and maintained their characteristic phenotypes (cell culture in Chapter 8.1).

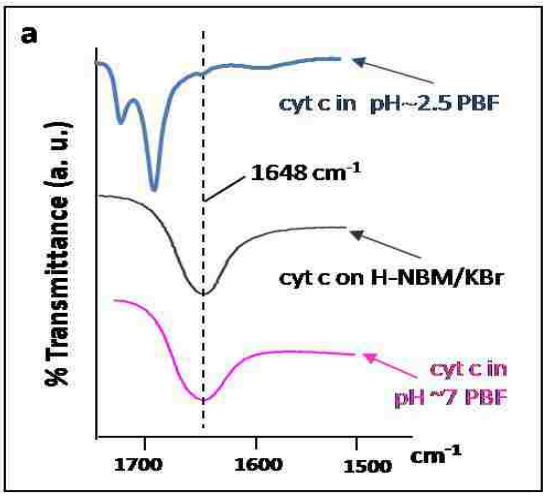

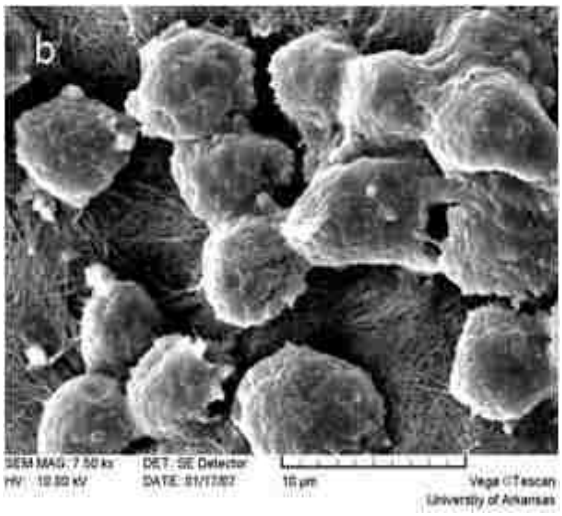

Figure 10.1 (a) FT-IR spectra. Black: cyt c -titanate-nanobelts mixed with KBr; pink: cyt c in the pH 6.8 buffer solution; blue: cyt c in pH ~2.5 buffer solution. (b) SEM image of the PC-12 cells grown on hydrogen titanate-nanobelts scaffolds for 72 h.

10.3 Greatly Enhanced Electron Transfer on the Nanobelt Scaffold

It is believed that the adsorption of cyt c on the titanate-nanobelts can be attributed mainly to the electrostatic effect. At the pH 6.2–9, the H-titanate nanobelt surface is negatively charged because of its isoelectric point of 6.2[128], while the cyt c surface is positively charged due to its isoeletcric point of 10–10.5. Thus, the negative titanate-nanobelt surface has a high affinity to the positive charged cyt c . Moreover, the cyt c shape in aqueous solution is nearly spherical (a × b × c = 1.5 nm × 1.7 nm × 1.7 nm),[129] and easily included into the voids (the size of holes: over 500 nm^2) of the entangled titanate-nanobelts so as to further enhance the retention of the cyt c folding during the electrochemical redox processes.

The scaffolding titanate-nanobelts can offer a desirable environment for the cyt c to undergo facile electron-transfer reactions. The electrochemical redox reaction of the cyt c between Fe (III) and Fe(II) was characterized by means of the CV. Figure 10.2 showed the CV data from an ITO glass electrode coated with the titanate-nanobelt (red) and the cyt c -titanate-nanobelts (blue), respectively, in a potassium phosphate buffer solution (pH 6.8). In Figure 10.2, a pair of reversible and well defined redox peaks from the cyt c -titanate-nanobelt electrode together with the formal peak potential (E^0) of ~ 0.03 V have been recorded. The E^0 is calculated from an average of anodic peak's and cathodic peak's potential values, according to the general equation

$$E^0 = \frac{1}{2}(E_{pc} + E_{pa})$$

where the E_{pc} and E_{pa} represent cathodic peak potential and anodic peak potential, respectively. The E^0 value (~ 0.03 V) is close to that reported by other researchers.[130]

Measurement of the faradic current as a function of scan rate can help diagnose whether a redox reaction on the electrode surface is controlled by diffusion. Figure 10.3a shows CV curves of the cyt c -titanate-nanobelt-modified electrode in the pH 6.8 at various scan rates. At a low scan rate (< 0.05 V/s), the redox peaks were weak and broad. As the scan rate was increased, the redox peaks became strong and sharp. Figure 10.3b display that the cathodic and the anodic peaks are both linearly proportional to the scan rate from 0.01 V/s to 0.2 V/s, implying that such an electrode has the typical characteristic of the thin-layer electrochemistry.[131]

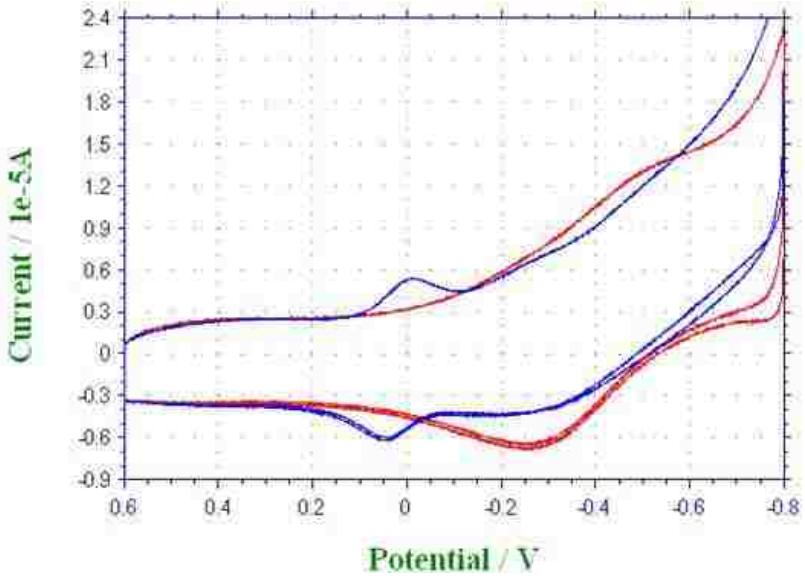

Figure 10.2 CV plots from the ITO glass electrodes modified with titanate-nanobelts (red), 450 picomoles of cyt c on the titanate-nanobelts (blue) in pH 6.8 buffer solutions. scan rate: 0.2 V/s.

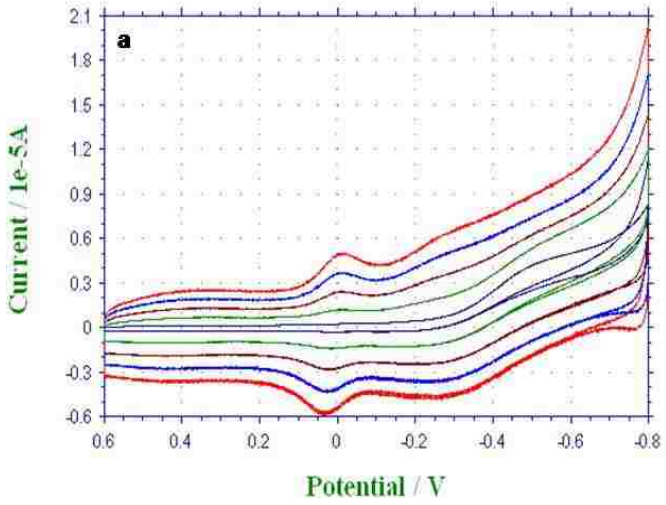

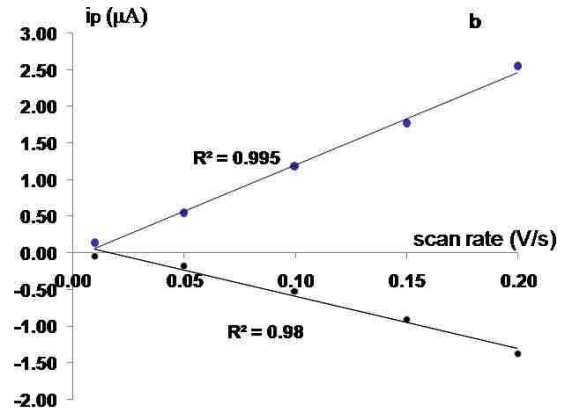

Figure 10.3 (a) Scan rates (V/s) for the sample with 450 picomoles of cyt c . Red, 0.2; Blue, 0.15; Dark red, 0.1; Green, 0.05; Dark blue, 0.01 in pH 6.8 buffer solution. (b) the relationship between the scan rate and the i_{pa} (blue spotted line) and i_{pa} (black spotted line).

The sensing of the cyt c anchored inside the bioscaffold was conducted at the pH 6.8. As the concentration the cyt c was increased, the voltammetric current was increased linearly. Figure 10.4a shows cyclic voltammegrams at different concentrations of cyt c and Fig.10.4b represents the relationship between the concentration of the protein and the current of the anodic peak. The reversible, well-defined voltammetric signals were observed from 15 µL solution in the concentration range from 3.0 µM (or 45 picomoles) to 30.0 µM (or 450 picomoles). The concentrations were all linearly (R^2 = 0.996) correlated with the anodic currents, as shown in the Fig 10.4b. The equation for straight line is y = -0.004x + 0.3287. The standard derivation of slop (Sm) and intercept (Sb)[132] are 0.00018 and 0.0568. The limit of detection (LOD) is 42.6 pmoles.

10.4 Sensing Cyt c Using the Square-Wave Voltammetry (SWV)

The electron-transfer activity of cyt c immobilized on the titanate-nanobelts was studied by the square-wave voltammetry, because the SWV is commonly regarded as a powerful electrochemical technique for characterizing the confined interfacial molecules.[133] The SWV curve of cyt c -titanate-nanobelts in the pH 6.8 buffer solution is shown in Figure 10.5a, with the high signal-to-noise ratio and resolution. In addition, the peak current is linearly correlated with the frequencies (see Figure 10.5b).

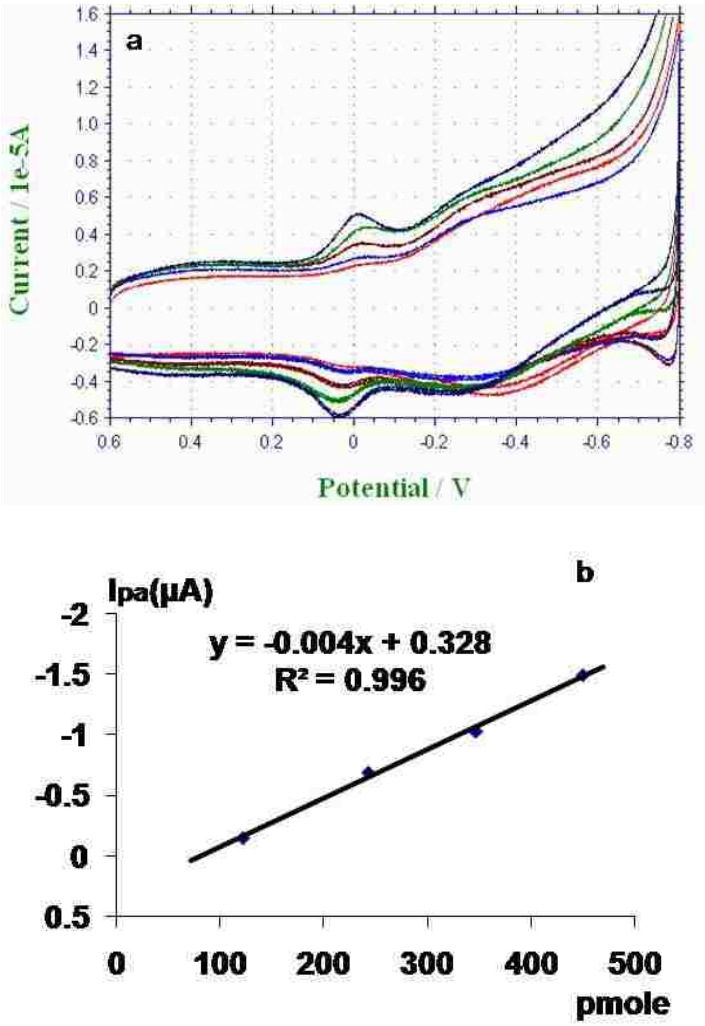

Figure 10.4 (a) CV (scan rate of 0.2 Vs^{-1}) obtained from various cyt c concentrations in the pH 6.8 buffer solution. dark blue, 450 picomoles; green, 347 picomoles; dark red, 243 picomoles; blue, 122 picomoles; and red, 45 picomoles. (b) The relationship between the concentrations and the i_{pa}.

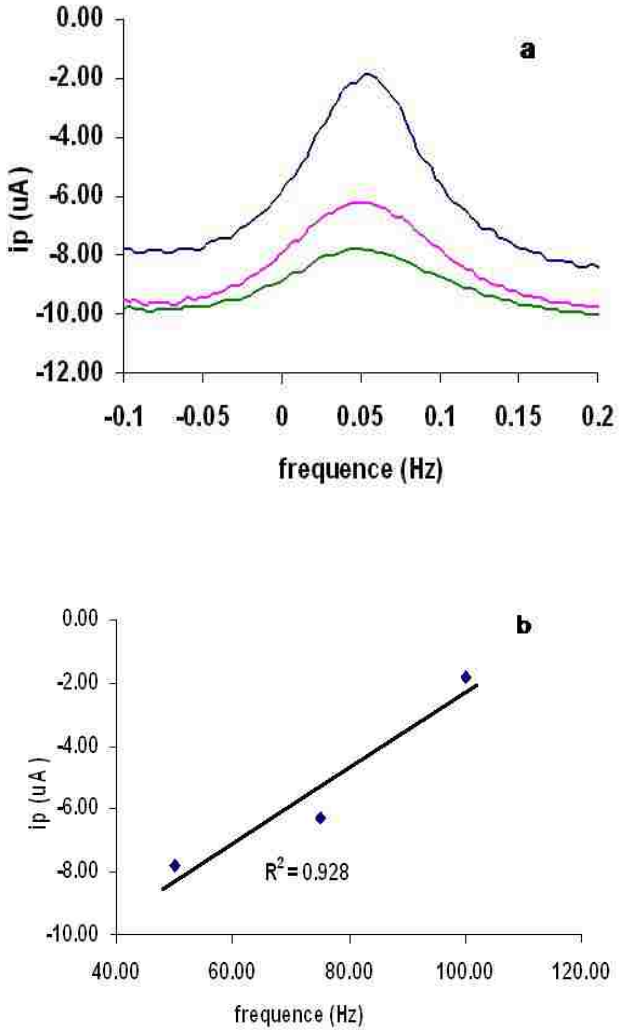

Figure 10.5 Square-wave voltammogram (SWV) study. (**a**) SWV of the 450 picomoles cyt c -titinate-nanobelt in the pH 6.8 buffer solution. SWV conditions: equilibration time, 2s; Potential amplitude, 25 mV; step height, 4mV, and frequencies of 50 (green), 75 (pink), 100 (blue) Hz. (**b**) The relationship between the frequencies and i_p data.

10.5 The Lattice–Intercalation Effect on Detecting Protein Cyt c

To detect the influence of electron transfer of cation exchanged nanobelt for protein, the protein cyt c was used. Figure 10.6 represents a linear relationship between the nanobelt d-space and the formal potentials (E°) of the cyt c . The formal potentials (E°) were obtained from cyclic voltammetry in the pH 6.8 PBS solution. The cyt c (450 pmoles) immobilized on the surface of the H^+– exchanged nanobelts, Li^+– exchanged nanobelts, and Na^+– exchanged nanobelts pre-modified on ITO electrodes. The formal potentials (E°) of the cyt c show well-fitted linear correlation that the more negative formal potential (E°) appearing on the larger d-spaced nanobelts with a trend of E°(Na–nanobelt membrane) > E° (Li–nanobelt membrane) > E° (H–nanobelt membrane). There are two possible reasons may cause this phenomenon. One is the different band gaps for H^+–nanobelts (3.3 ev) and Na^+–nanobelts (3.4 ev) that cause difficulty in electron transfer with the increasing interlayer distance.[134] The other may base on difference of the surface properties of the cation-exchanged nanobelts such as the point of zero charge (PZC). The H^+– exchanged nanobelts has a lower PZC (~4.1) based on our experiments in chapter 9 compared with that of Na^+– exchanged nanobelts (~ 9.8). Therefore, the surface environment of H^+– exchanged nanobelts is more favorable for electrostatic effect, and then the redox reaction of cyt c on the H^+–nanobelts' surface is easier compared with cyt c immobilized on the Na^+–nanobelts.

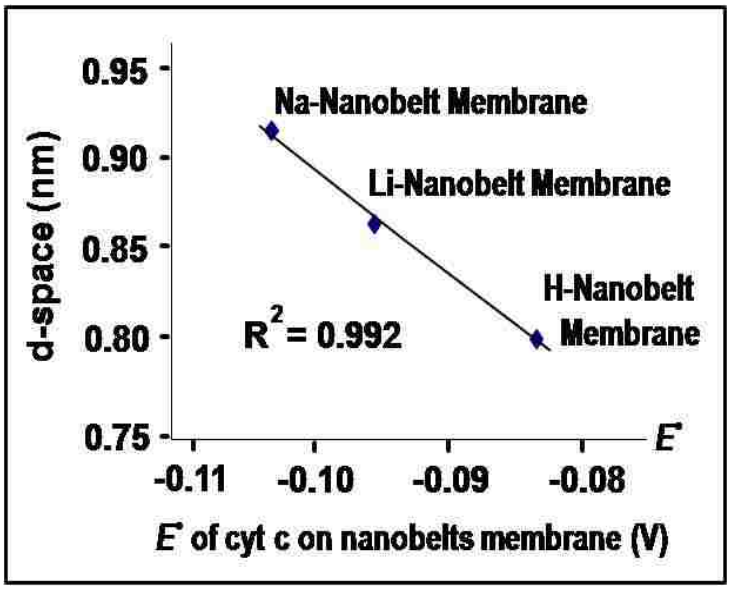

Figure 10.6 A linear relationship between the formal potential of the cyt c on the various cation exchanged nanobelt membrane and the XRD d-space of the intercalated nanobelts

10.6 Conclusion

In summary, the titanate-NB-based bioscaffold can be used as a versatile sensing platform for detecting biomolecules simply and quickly. The FT-IR result and neuron cells growth demonstrate the biocompatibility of the titanate-NBs scaffolds. The electrochemical results illustrate the fast electron transfer through the titanate-NBs scaffolds. The detection limit is 45 pmols that represents high sensitivity of the titanate-NBs modified electrode. This work may serve as a proof of a new concept that sensing biomolecules inside such a bioscaffold is doable.

Chapter 11.

Sensing Dopamine (DA) on Membrane Scaffold of H–Titanate Nanobelts

11.1 Electrochemical Sensing of Dopamine (DA) on H-titanate Nanobelts

In Figure 11.1, the blue line is cyclic voltammogram (CV) of the H-titanate nanobelts modified on glassy carbon (GC) electrode in pH 6.78 phosphate buffer solution (PBS) solution without DA; the red line is CV of DA immobilized on the H-titanate nanobelts modified GC electrode in pH 6.78 PBS solution. The concentration of DA was 0.21 mM; scan rate was 0.1 V/s. The scan started from negative voltage (-0.8V) to positive voltage (0.6V). Comparing two CVs, with and without DA, two pair of peaks observed from CV of DA.

The two pairs of peaks represent the redox reactions of DA on the nanobelts modified GC electrode. The pair of A peak and B peak were determined the redox reaction of dopamine (A) and dopaminequinone (B);[135] then the dopaminequinone (B) was changed to leucodopachrome (C) [136] on the electrod surface; the pair of C peak and D peak were represented the redox reaction of leucodopachrome (C) and dopachrome (D).[136] The CV shows that DA redox reaction is electrode process, irreversible chemical reaction, and electrode process (ECE).

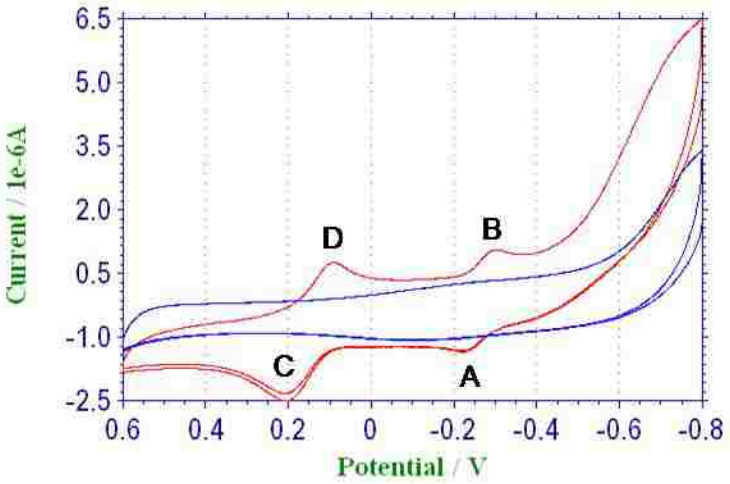

Figure 11.1 CV plots at pH 6.78 PBS from the GC electrodes modified with titanate-nanobelts (blue, without DA) and 0.21 mM DA on the titanate nanobelts (red). scan rate: 0.1 V/s

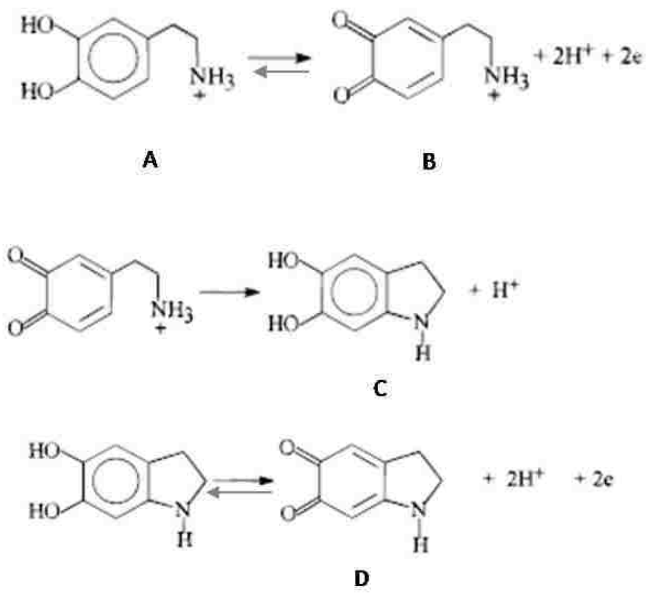

The effect of scan rate on CV was studied. The scan rates were changed from 0.01 to 0.2 (V/s). The redox peaks (A and B) were monitored during the changing scan rates. Figure 11.2a represents the CVs at various scan rates as the concentration of dopamine was 0.21 mM in PBS at pH 6.78. Figure 11.2b shows the relationship between the square root of scan rate ($v^{½}$) and current peaks. The straight lines were obtained from cathodic currents and anodic currents. The currents were increased as the square root of scan rates increased. This behavior showed the reversible redox reaction of dopamine on the potassium nanobelt modified GC electrodes.

The pH value is one of the parameters that may influence the formal potential and peak currents of redox reaction. Solutions with different pH values were prepared in PBS buffer to study the effect of pH. Figure 11.3a shows the CVs of DA in solutions with different pH values. The formal potentials (E°) are monitored from peak C and peak D. The formal potential (E°) is calculated using

$E^{\circ} = (E_{pa} + E_{pc})/2$.[131] From figure 11.3a the formal potentials (E°) are found to be 0.196 V at pH 5.48, 0.146 V at pH 6.78, and 0.121 V at pH 7.39 respectively. Figure 11.3b demonstrates that the relationship between formal potentials (E°) and pH values is a straight line. The formal potentials (E°) calculated from C and D decrease with increasing pH. The peak current is also found to reduce with increasing pH of solution. These behaviors indicate that the formal potential is the pH dependent. In Figure 11.3a, the CV also shows that the current peaks of A and B are increased as the pH values increases. This phenomenon demonstrates that higher pH is more favorable for the redox reaction of A (dopamine) and B (dopaminequinone). As the pH values are increased, the concentrations of hydroxide [OH^-] increases. The concentration of proton [H^+] decreases due to neutralization thereby shifting the equilibriums of reactions from A to B. The effect of concentration on electrochemical current can be given by the Randles-Sevick equation, $i_p[= (2.69\times10^5)n^{3/2}AD^{1/2}\nu^{1/2}C^*]$.[131]

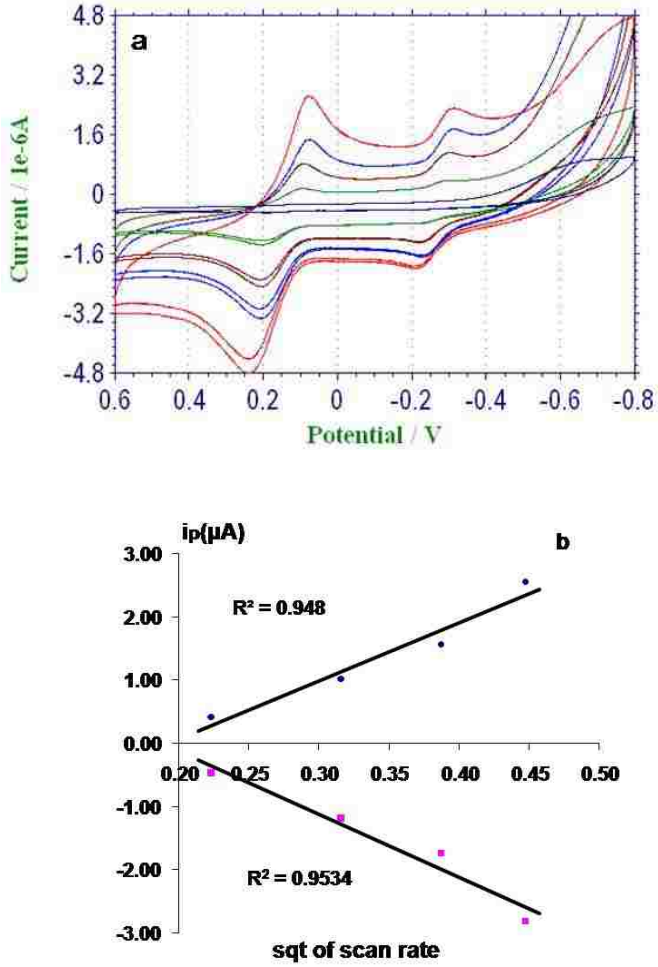

Figure 11.2 (a) Scan rate (V/s) changes for the sample of 0.21mM DA on the nanobelt modified GC electrodes. red, 0.2; blue, 0.15; dark red, 0.1; green, 0.05; dark blue, 0.01 at pH of 6.78 PBS (b) The relationship between the square root of scan rate and the i_{pc} (blue)and i_{pa} (pink)at pH 6.78 PBS

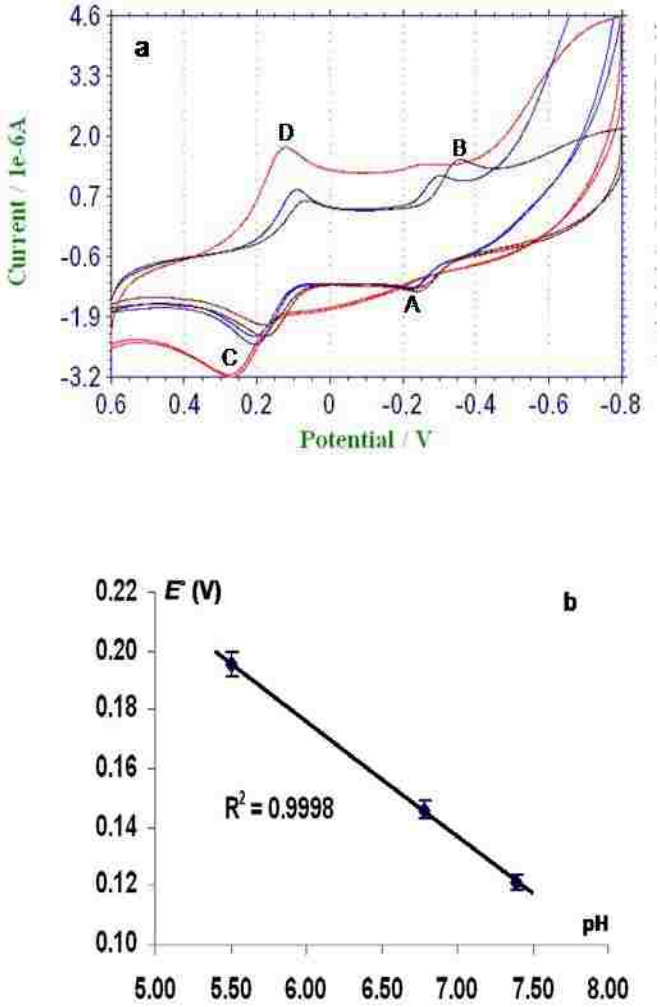

Figure 11.3 (a) the CV of DA / H-titanate nanobelt / GC electrodes at different pH: red: pH 5.48; blue: pH 6.78; dark red: 7.39 at 0.21mM DA (b) the relationship between pH and formal potentials

The CV behavior as a function of the concentration of DA is investigated. Figure 11.4a shows the CVs of the dopamine in pH 6.8 PBS at various concentrations. The peak at 0.14 V was monitored for the detection of dopamine. Figure 11.4b determines the relationship of DA concentrations with anodic current peaks (i_{pa}) and cathodic current peaks (i_{pc}). From Figure 11.4b, the i_{pa} and i_{pc} increase lineally as the concentrations increase. This result suggests that the fraction of DA immobilized on the H-titanate nanobelt which modified on GC is a constant at all concentration levels.

11. 2 Sensing DA by Differential Pulse Voltammogram (DPV)

The detection of dopamine was studied by using differential pulse voltammetry. (DPV). The DPVs of dopamine at various concentrations are showed in Figure 11.5a. Two peaks are observed. The peak at 0.14 V was monitored for the detection of dopamine. Figure 11.5b exhibits a linear relationship between the peak current and concentration. Comparing the results of CV and DPV at different concentrations in pH 6.78 PBS solution, DPV is found to be a more sensitive technique than CV for the detection of dopamine.

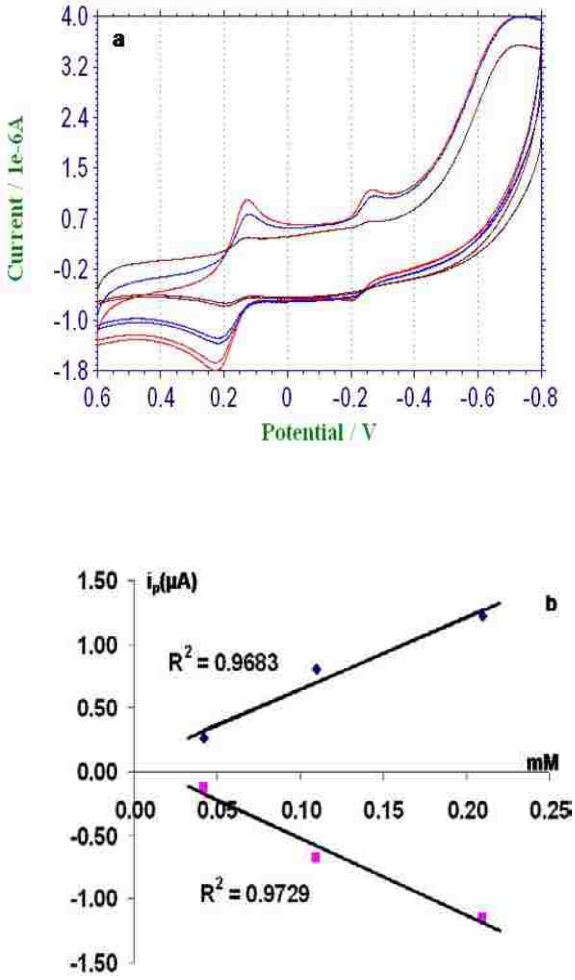

Figure 11.4 **(**a) CV obtained from various DA concentrations on the nanobelt modified GC electrodes in the pH 6.78 PBS at scan rate of 0.1 V/s. dark red: 42.2 μM; blue: 0.11 mM; red: 0.21 mM (b) Relationship between concentration and i_{pa} and i_{pc}

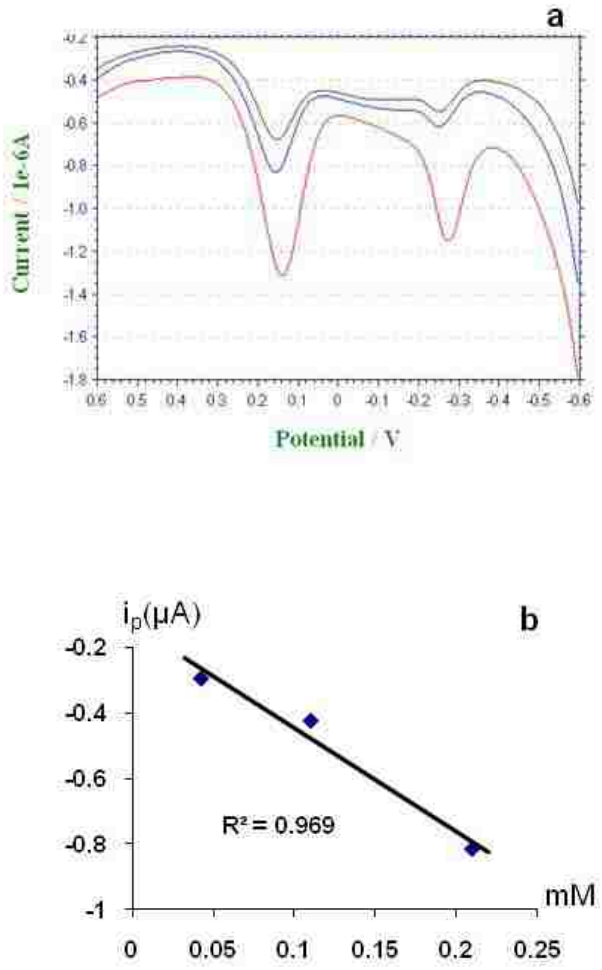

Figure 11.5 (a) DPV studied on the nanobelt modified GC electrodes in pH 6.78 PBS solution at various concentrations: dark red: 42.2 μM; blue: 0.11 mM; red: 0.21 mM. DPV conditions: amplitude 0.05 V; pulse width = 0.05 s: sample width = 0.0167 s; pulse period = 0.2 s. (b) The relationship between the concentrations and the i_p

11.3 Conclusion

We developed the biosensor that can detect dopamine using H– titanate NB modified glassy carbon electrode combines with electrochemical methods such as CV and DPV. The detected lowest concentration is 42.2 μM. The formal potentials (E°) of dopamine decrease as the pH values increase. The biocompatibility of H– titanate NB is also studied by growing pheochromocytoma cells (PC-12 cells) on the surface of H–titanate NB. Our results show that the PC-12 are attached well and grown on the H–titanate NB successfully without coating any media on the surface of H–titanate NB. These results demonstrate that the biomaterial of H–titanate NB offers the great opportunities for nerve tissue engineering and development of biomedical devices.

References:

1. http://www.azonano.com/details.asp?ArticleID=1174

2. Y. Cui, Q. Wei, H. Park, C. M. Lieber. "Nanowire nanosensors for highly sensitive and selective detection of biological and chemical species" *Science* 2001, 293, 1289-1292

3. S. Jin, D. Whang, M. C. McAlpine, R. S. Friedman, Y. Wu, C. M. Lieber. "Scalable interconnection and integration of nanowire devices without registration" *Nano. Lett*. 2004, 4, 915-919

4. Z. L. Wang. "Towards self-powered nanosystems: From nanogenerators to nanopiezotronics" *Adv. Mater*. 2008, 18, 3553-3567

5. R. J. Chen, S. Bangsaruntip, K. A. Drouvalakis, N. W. S. Kam, M. Shim, Y. Li, W. Kim, P. J. Utz, H. Dai. "Noncovalent functionalization of carbon nanotubes for highly specific electronic biosensors" *Proc. Natl. Acad. Sci. USA*. 2003 100, 4984–4989

6. B. G. Chung, L. Kang, A. Khademhosseini. "Micro- and nanoscale technologies for tissue engineering and drug discovery applications" *Expert Opin. Drug Discov*. 2007, 2, 1-16

7. B. M. Baker, A. M Handorf, L. C Lonescu, W.-J. Li, R. L Mauck. "New directions in nanofibrous scaffolds for soft tissue engineering and regeneration" *Expert Rev. Med. Devices* 2009, 6, 515-532

8. W. C. Chang, M. Kliot, D. Sretavan. "Microtechnology and Nanotechnology in nerve repair" *Neurol Res*. 2008, 30, 1053-1062

9. A. Subramanian, U. M. Krishnan, S. Sethuraman. "Development of biomaterials scaffold for nerve tissue engineering: biomaterial mediated neural regeneration" *J. Biomed. Sci*. 2009, 16: 108

10. J. Lee, M. J. Cuddihy, N. A. Kotov. "Three-Dimensional Cell Culture Matrices: State of the Art" *Tissue Engineering Part B*. 2008, 14, 61-86

11. P. X. Ma, R. Zhang. "Synthetic nano-scale fibrous extracellular matrix" *J. Biomed. Mater. Res. Part A* 1999, 46, 60-72

12. W. Potter, R. E. Kalil, W. J. Kao. "Biomimetic material systems for neural progenitor cell-based therapy" *Front. Biosci.* 2008, 13, 806-821

13. A. I Teixeira, J. K Duckworth, O. Hermanson. “Getting the right stuff: Controlling neural stem cell state and fate *in vivo* and *in vitro* with biomaterials” *Cell Res.* 2007, 17, 56-61

14. R. G. Ellis-Behnke, Y–X. Liang, S.-W. You, D. K. C. Tay, S. Zhang, K.-F. So, G. E. Schneider. “Nano neuro knitting: Peptide nanofiber scaffold for brain repair and axon regeneration with functional return of vision” *Ptoc. Natl. Acad. Sci. USA* 2006, 103, 5054-5059.

15. H. S. Koh, T. Yong, C.K. Chan, S. Ramakrishna. “Enhancement of neurite outgrowth using nano-structured scaffolds coupled with laminin” *Biomaterials* 2008, 29, 3574-3582.

16. S. Patel, K. Kurpinski, R. Quigley, H. Gao, B. S. Hsiao, M.-M. Poo, S. Li. “Bioactive Nanofibers: Synergistic Effects of Nanotopography and Chemical Signaling on Cell Guidance” *Nano. Lett*. 2007, 7, 2122-2128.

17. J. M. Corey, D. Y. Lin, K. B. Mycek, Q. Chen, S. Samuel, E. L. Feldman, D. C. Martin. “Aligned electrospun nanofibers specify the direction of dorsal root ganglia neurite growth” *J. Biomed. Mater. Res. Part A* 2007, 83a, 636-645

18. J. Xie, M. R. MacEwan, A. G. Schwartz, Y. Xia. “Electrospun nanofibers for tissure engineering” *Nanoscale* 2010, 2, 35-44

19. J. Xie, S. M. Willerth, X. Li, M. R. Macewan, A. Rader, S. E. Sakiyama-Elbert, Y. Xia. “The differentiation of embryonic stem cells seeded on electrospun nanofibers into neural lineages” *Biomaterials* 2009, 30, 354-362

20. G. T. Christopherson, H. Song, H.-Q. Mao. “The influence of fiber diameter of electrospun substrates on neural stem cell differentiation and proliferation” *Biomaterial* 2009, 30, 556-564

21. S. Ogura, M. Kohno, K. Sato, Y. Inoue. “Photocatalytic properties of $M_2Ti_6O_{13}$ (M=Na, K, Rb, Cs) with rectangular tunnel and layer structures: behavior of a surface redial produced by UV irradiation and photocatalytic activity for water decomposition” *Phys. Chem..Chem. Phys*. 1999, 1, 179-183

22. A. Nakahira, W. Kato, M. Tamai, T. Isshiki, K. Nishio, H. Aritani. “Synthesis of nanotube from a layered $H_2Ti_4O_9 \bullet H_2O$ in a hydrothermal treatment using various titania sources” *J. Mater. Sci*. 2004, 39, 4239-4245

23. C. C. Tsai, H. Teng. “Regulation of the physical characteristics of titania nanotube aggregates synthesized from hydrothermal treatment” *Chem. Mater*. 2004, 16, 4352-4358

24. S. H. Lim, J. Z. Luo, Z.Y. Zhong, W. Ji, J. Y. Lin. “Room-temperature hydrogen uptake by TiO2 nanotubes” *Inorg. Chem.,* 2005, 44, 4124-4126

25. J. R. Li, Z. L. Tang, Z. T. Zhang . “H-titanate nanotube: a novel lithium intercalation host with large capacity and high rate capability” *Electrochem. Commun*. 2005, 7, 62-67

26. B. L. Wang, Q. Chen, J. Hu, H. Li, Y.F. Hu, L.M Peng. “Synthesis and characterization of large scale potassium titanate nanobelts with good Li-intercalation performance” *Chem. Phys. Lett.* 2005, 406, 95-100

27. P. Hoyer. “Formation of a titanium dioxide nanotube array” *Langmuir* 1996, 12, 1411-1413

28. H. Imai, Y. Takei, K. Shimizu, M. Matsuda, H. Hirashima. “Direct preparation of anatase TiO2 nanotubes in porous alumina membranes” *J. Mater. Chem.* 1999, **9**, 2971-2972

29. M. Zhang, Y. Bando, K. Wada. “Sol-gel template preparation of TiO2 nanotubes and nanorods” *J. Mater. Sci. Lett.* 2001, 20, 167-170

30. S. Kobayashi, K. Hanabusa, N. Hamasaki, M. Kimura, H. ShiraiSeiji Shinkai. “Preparation of TiO2 hollow-fibers using supermolecular assemblies” *Chem. Mater*. 2000, 12, 1523-1525

31. R. A. Caruso, J. H. Schattka, A. Greiner. “Titanium Dioxide Tubes from Sol-Gel Coating of Electrospun Polymer Fibers” *Adv. Mater.* 2001, 13, 1577-1579

32. D. Gong, C. A. Grimes, O. K. Varghese, Z. Chen, W. Hu, E.C. Dickey. “Titanium oxide nanotube arrays prepared by anodic oxidation” *J. Mater. Res*. 2001, 16, 3331-3334

33. C. Ruan, M. Paulose, O. K. Varghese, G. K. Mor, C. A. Grimes. “Fabrication of highly ordered TiO_2 nanotube arrays using as organic electrolyte” *J. Phys. Chem. B.* 2005, 109, 15754-15759

34. J. M. Macak, K. Sirotna, P. Schmuki. “Self-organized porous titanium oxide prepared in Na_2SO_4/NaF electrolytes” *Electrochim. Acta* .2005, 50, 3679-3684

35. Q. Chen, L–M. Peng. “Structure and applications of titanate and related nanostructures” *Int. J. Nanotech.* 2007, 4, 44-65

36. D. V. Bavykin, J.M. Friedrich, F, C. Walsh. “Protonated titanates and TiO_2 nanostructured materials: synthesis, properties, and applications” *Adv. Mater.* 2006, 18, 2807-2824

37. X. G. Xu, X. Ding, Q. Chen, L–M. Peng. “Electronic, optical, and magnetic properties of Fe-intercalated H2Ti3O7 nanotubes: First-principles calculations and experiments” *Phys. Rev. B.* 2006, 73, 165403

38. R. Z. Ma, T. Sasaki, Y. Bando. “Alkali metal cation intercalation properties of titanate nanotubes” *Chem. Commun.* 2005, 7, 948-950

39. X. M. Sun, Y. D. Li. “Synthesis and characterization of ion-exchangeable titanate nanotubes” *Chem-Eur. J* 2003, 9, 2229-2238

40. H. Zhu, X. Gao, Y. Lan, D. Song, Y. Xi, J. Zhao. “Hydrogen titanate nanofibers covered with anatase nanocrystals: a delicate structure achieved by the wet chemistry reaction of titanate nanofibers” *J. Am. Chem. Soc.*, 2004, 126, 8380–8381

41. M. Hodos, E. Horváth, H. Haspel, Á. Kukovecz, Z. Kónya, I. Kiricsi. “Photosensitization of ion-exchangeable titanate nanotubes by CdS nanoparticles” *Chem. Phys. Lett.* 2004, 399, 512-515

42. D. V. Bavykin, E. V. Milsom, F. Marken, D. H. Kim, D. H. Marsh, D. J. Riley, F. C. Walsh, K. H. El-Abiary, A. A. Lapkin. “A novel cation-binding TiO_2 nanotube substrate for electro- and bioelectro-catalysis” *Electrochem. Commun.* 2005, 7, 1050-1058

43. D. V. Bavykin, A. A. Lapkin, P. K. Plucinski, J. M. Friedrich, F. C. Walsh. “TiO_2 nanotube-supported ruthenium(III) hydrated oxide: A highly active catalyst for selective oxidation of alcohols by oxygen” *J. Catal.* 2005, 235, 10-17

44. D. V. Bavykin, A. A. Lapkin, P. K. Plucinski, J. M. Friedrich, F. C. Walsh. “Reversible storage of molecular hydrogen by sorption into multilayered TiO2 nanotubes” *J. Phys. Chem. B* 2005, 109, 19422-19427

45. F. Patolsky, G. Zheng, C. Lieber. “Nanobelt sensors for medicine and the life sciences” *Nanomedicine* 2006, 1, 51-56.

46. F. Patolsky, G. Zheng, C. M. Lieber. “Fabrication of silicon nanobelt devices for ultrasensitive, label-free, real-time detection of biological and chemical species” *Nature protocols* 2006, 1, 1711-1724.

47. P. Alivisatos. “The use of nanocrystals in biological detection” *Nat. Biotechnal*. 2004, 22, 47-52.

48. X. Gao, Y. Cui, R. M. Levenson, L. W. K. Chung, S. Nie “In vivo cancer targeting and imaging with semiconductor quantum dots” *Nat. Biotechnal*. 2004, 22, 969-976.

49. A. Fujishima, K. Honda. “Electrochemical photolysis of water at a semiconductor electrode” *Nature* 1972, 238, 37-38.

50. B. O’Regan, M. Grätzel. “A low-cost, high-efficiency solar cell based on dye-sensitized colloidal TiO_2 films” *Nature* 1991, 353, 737-740.

51. T. Nagaura, K. Tozawa. “Lithium ion rechargeable battery” *Prog. Batteries Sol. Cells*. 1990, 9, 209-217.

52. J. M. Tarascon, M. Armand. “Issues and challenges facing rechargeable lithium battries” *Nature* 2001, 414, 359-367.

53. Z. L. Wang. “Towards self-powered nanosystems: From nanogenerators to nanopiezotronics” *Adv. Funct. Mater.* 2008, 18, 1-15

54. Z. W. Pan, Z. R. Dai, Z. L. Wang. “Nanobelts of semicondecting oxides’’ *Science* 2001, 291, 1947-1949

55. F. Patolsky, G. Zheng, O. Hayden, M. Lakadamyali, X.W. Zhuang, L. M. Charles. “Electrical detection of signal viruses” *Proc. Natl. Acad. Sci. USA* 2004, 101, 14017-14022.

56. A. Riss, T. Berger, H. Grithe, J. Bemardi, O. Diwaid, E. Knözinger. “Chemical control of photoexcited states in titanate nanostructrures” *Nanolett*. 2007, 7, 433-438.

57. X. G. Xu, X. Ding, Q. Chen, L–M. Peng “Modification of electronic, optical, and magnetic properties of titanate nanotubes by metal intercalation” *Phys. Rev. B* 2007, 75, 035423(12)

58. X. Sun, Y. Li. “Synthesis and characterization of ion-exchangeable titanate nanotubes” *Chem. Eur. J*. 2003, 9, 2229-2238.

59. J. Li, Z. Tang, Z. Zhang. “Layered hydrogen titanate nanobelts with novel lithium intercalation properties” C*hem. Mater*. 2005, 17, 5848-5855.

60. D. V. Bavykin, J. M. Friedrich, F. C. Walsh. “Protonated titanates and TiO_2 nanostructured materials: synthesis, properties, and applications” *Adv. Mater*. 2006, 18, 2807-2824.

61. A. K. Wanekaya, W. Chen, N. V. Myung, A. Mulchandani. “Nanobelt-based electrochemical biosensors” *Electroanalysis* 2006, 18, 533-550

62. S. Zhang, G. Wright, Y. Yang. “Materials and techniques for

electrochemical biosensor design and construction" *Biosens. Bioelectron*. 2000, 15, 273-282.

63. M. Mehrvar, M. Abdi. "Recent developments, characteristics, and potential applications of electrochemical biosensors" *Anal. Sci*. 2004, 20, 1113-1126.

64. M. Gerard, A. Chaubey, B..D. Malhotra. "Application of conducting polymers to biosensors" *Biosens. Bioelectron*. 2002, 17, 345-359.

65. Q. Zhao, Z. Qan, Q. Zhuang. "Electrochemical sensors based on carbon nanotubes" *Electroanalysis* 2002, 14, 1609-1613.

66. C. Mousty. "Sensors and biosensors based on clay-modified electrodes — new trends" *Appl. Clay. Sci*. 2004, 27, 159-177.

67. F. Millett, B. Durham. "Chemical modification of surface residues on Cytochrome c" *Cytochrome c A multidisciplinary approach* University science book 1996, chapter 17, p573-591.

68. H–J.Kim, K–S. Lee, M–S Won, Y–B. Shim. "Characterization of protein-attached conducting polymer monolayer" *Langmuir* 2008, 24, 1087-1093.

69. J–W. Shie, U. Yogeswaran, S–M. Chen. "Electroanalytic properties of cytochrome c by direct electrochemistry on multi-walled carbon nanotubes incorporated with DNA biocomposite film" *Talanta* 2008, 74, 1659-1669.

70. C. Lei, F. Lisdat, U. Wollenberger, F. W. Scheller. "Cytochrome c /clay-modified electrode" *Eectroanalysis* 1998, 11, 274-276.

71. F. Patolsky, B. P. Timko, G. Zheng, C. M. Leber. "Nanowire-based nanoelectromic devices in the life sciences" *MRS Bulletin* 2007, 32, 142-149

72. J. Li, Y. Lu, Q. Ye, M. Cinke, J. Han, M. Meyyappan. "Carbon nanotube sensors for gas and organic vapor detection" *Nano Lett*. 2003, 3, 929-933

73. A. Star, T. R. Han, J. C. P. Cabriel, K. Bradley, G. Gruner. "Interaction of aromatic compounds with carbon nanotubes: correlation to the hammett of the substituent and measured carbon nanotube FET response" *Nano Lett*. 2003, 3, 1421- 1423

74. E. S. Snow, F. K. Perkins, E. J. Houser, S. C. Badescu, T. L. Reinecke. "Chemical detection with a single-walled carbon nanotube capacitor" *Science* 2005, 307 1942-1945

75. Z. Liu, X. Sun, N. Nakayama, H. Dai. "Supramolecular chemistry on water-soluble carbon nanotubes for Drug loading and delivery" *ACS Nano.* 2007, 1, 50-56

76. M. L. Schipper, N. Nakayama-Rarchford, C. R. Davis, N. W. S. Kam, P. Chu, Z. Liu, X. Sun, H. Dai, S. S. Gambhir, "A pilot toxicology study of single walled carbon nanotubes in a small sample of mice" *Nat. Nanotech.* 2008, *3,* 216 -221

77. H. R. Byon, H. C. Choi. "Network single-walled carbon nanotube-field effect transistors (SWNT-FETs) with increased schottky contact area for highly sensitive biosensors applications" *J. Am. Chem. Soc.* 2006, 128, 2188-2189

78. D. A. Heller, S. Baik, T. E. Eurell, M. S. Strano. "Single-walled carbon nanotube spectroscopy in live cells: Towards long-term labels and optical sensors" *Adv. Mater.* 2005, *17,* 2793-2799.

79. K. Welsher, Z. Liu, D. Daranciang, H. Dai. "Selective Probing and Imaging of Cells with Single Walled Carbon Nanotubes as Near-Infrared Fluorescent Molecules" *Nano Lett.* 2008, 8, 586-590.

80. P. Cherukuri, S. M. Bachilo, S. H. Litovsky, R. B. Weisman. "Near-infrared Fluorescence microscopy of single-walled carbon nanotubes in phagocytic cells" *J. Am. Chem. Soc.* 2004, 126, 15638-15639.

81. T. Paunesku, T. Rajh, G. Wiederrecht, J. Maser, S. Vogt, N. Stojievi, M. Proti, B. Lai, J. Oryhon, M. Thurnauer, G. Woloschak. "Biology of TiO2–Oligonucleotide nanocomposites" *Nature Mater.* 2003, 2, 343-346

82. M. Yang, J. Wang, H. Li, J-G. Zheng, N. N. Wu. "A lactate electrochemical biosensor with a titanate nanotube as direct electron transfer promoter" *Nanotechnology* 2008, 19, 075502

83. A. Lu. "Towards development of chemosensors and biosensors with metal-oxide-based nanobelts or nanotubes" *Biosens. Bioelectron*. 2008, 24, 167-177

84. Z. Li, H. Zhang, W. Zheng, W. Wang, H. Huang, C. Wang, A. G. MacDiarmid, Y. Wei. "Highly sensitive and stable humidity nanosensors based on LiCl doped TiO2 electrospun nanofibers" *J. Am. Chem. Soc.* 2008, 130, 5036-5037

85. Y. Wang, G. Du, H. Liu, D. Liu, S. Qin, N. Wang, C. Hu, X. Tao, J. Jiao, J. Wang, Z. L. Wang. "Nanostructured Sheets of Ti–O Nanobelts for Gas Sensing and Antibacterial Applications" *Adv. Func. Mater*. 2008, 18, 1131-1137

86. L. Zhang, Q. Zhang, J. Li. “Layered Titanate Nanosheets Intercalated with Myoglobin for Direct Electrochemistry” *Adv. Func. Mater*. 2007, 17, 1958-1965

87. L. Zhang, Q. Zhang, X. L, J. Li. “Direct electrochemistry and electrocatalysis based on film of horseradish peroxidase intercalated into layered titanate nano-sheets” *Biosens. Bioelectron*. 2007, 23, 102-106

88. A. Teleki, S. E. Pratsinis, K. Kalyanasundaram, P. I. Gouma. “Sensing of organic vapors by flame-made TiO2 nanoparticles” *Sens. Actuators B Chem*. 2006, 119, 683-690

89 F. Millett, B. Durham. “Kinetics of electron transfer within cytochrome bc1 and between cytochrome bc1 and cytochrome c” *Photosynthesis Res.* 2004, 82, 1-16

90 W. Dong, A. Cogbill, T. Zhang, S. Ghosh, Z. R. Tian. “Multifunctional catalytic nanowire membranes and the membrane-based 3D devices” *J. Phys. Chem. B.* 2006, 110, 16819-16822

91 M. L. A. V. Heien, A. S. Khan, J. L. Ariansen, J. F. Cheer, P. E. M Phillips, K. M. Wassum, R. M. Wightman. “Real-time measurement of dopamine fluctuations after cocaine in the brain of behaving rat” *Proc. Nati. Acad. Sci. U.S.A* .2005, 102, 10023-10028

92. http://en.wikipedia.org/wiki/Bragg_diffraction

93. http://serc.carleton.edu/research_education/geochemsheets/techniques/SEM.htm

94. http://www.purdue.edu/REM/rs/sem.htm

95. http://www.msm.cam.ac.uk/doitpoms/tlplib/tem/image_formation.php

96. P. B. Hirsch, A. Howie, R. B. Nicholson, D.W. Pashley, M. J. Whelan. “Eletron Microscopy of Thin Crystal” 2nd edition, *Krieger, Huntington, New York* (1977)

97. www.msel.nist.gov/Nanotube2/Practice%20GuideSection%202_TGA.pdf

98. http://orgchem.colorado.edu/hndbksupport/irtutor/IRtheory.pdf

99. http://www.nuance.northwestern.edu/keckii/ftir1.asp

100. A. J. Bard, L. R. Faulkner. “Electrochemical Methods. Fundamentals and Applications” 2nd ed; *Wiley: New York*, 2001.

101. J. Park, J. R. Regalbuto, "A Simple, Accurate Determination of Oxide PZC and the Strong Buffering Effect of Oxide Surfaces at Incipient Wetness" *J. Colloid Interface Sci*. 1995, 175, 239-252

102. S. M. Hussain, A. K. Javorina, A. M. Schrand, H. M. Duhart, S. F. Ali, J. J. Schlager. "The Interaction of Manganese Nanoparticles with PC-12 Cells Induces Dopamine Depletion" *Toxicol. Sci.* 2006, 92, 456-463

References:

103. D. M. Fryer, J. F. Harvey. *High Pressure Vessels*; 1st ed.; Chapman & Hall, 1998

104. D. Bavykin, F. C. Walsh. *Titanate and Titania Nanotubes: Synthesis, Properties and Applications (RSC Nanoscience and Nanotechnology)*; 1st ed.; Royal Society of Chemistry, 2009

105. Q. Chen, L. M. Peng. "Structure and applications of titanate and related nanostructures" *Int. J. Nanotechnology* 2007, 4, 44-65

106. F. A. Cotton, G. Wilkinson, *Basic Inorganic Chemistry* (John Wiley & Sons, Inc. 1976)

107. Z. R. Tian, Y. G. Yin, S. L. Suib, C. L. O'Young. "Effect of Mg^{2+} ions on the formation of todorokite type manganese oxide octahedral molecular sieves" *Chem. Mater.* 1997, 9, 1126-1133

108. S. Zhang, Q. Chen, L–M. Peng. "Structure and formation of $H_2Ti_3O_7$ nanotubes in an alkali environment" *Phys. Rev. B* 2005, 71, 014104.

109. J. I. Langford, A. J. C. Wilson. "Scherrer after Sixty Years: A Survey and Some New Results in the Determination of Crystallite Size," *J. Appl. Cryst.* 1978, 11, 102-113

110. W. Dong, A. Cogbill, T. Zhang, S. Ghosh, R. Z. Tian. "Multifunctional, catalytic nanowire membranes and the membranes-based 3D Devices" *J. Phys. Chem. B* 2006, 16819-16822

111. E. Morgado Jr, M. A..S. de Abreu, G. T. Moure, B. A Marinkovic, P. M Jardim, A..S. Araujo. "Effects of thermal traeatment of nanostructured trititanate on their crystallographic and textural properties" *Mater. Res. Bull.* 2007, 42, 1748-1760

112. E. Morgado Jr, M. A..S. de Abreu, G. T. Moure, B. A Marinkovic, P. M Jardim, A. S. Araujo. "Characterization of nanostructured titanates obtained by

alkali treatment of TiO_2–anatases with distinct crystal size" *Chem. Mater*. 2007, 19, 665-676

113. P. Umek, R. C. Korošec, B. Jančar, R. Dominko, D. Arčon. "The influence of the reaction temperature on the morphology of sodium titanate 1D nanostructures and their thermal stability" *J. Nanosci. Nanotechnol*. 2007, 7, 3502-3508

114. O. P. Ferreira, A. G. S. Filho, J. M. Filho, O. L. Alves. "Unveiling the structure and composition of titanium oxide nanotubes through ion exchange chemical reactions and thermal decomposition processes" *J. Braz. Chem. Soc*. 2006, 17, 393-402

115. T. P. Feist, P. K. Davies. "The soft chemical synthesis of TiO2 (B) from layered titanates" *J. Solid State Chem.* 1992, 101, 275-295

116. J. Park, J. R. Regalbuto. "A simple, accurate determination of oxide PZC and the strong buffering effect of oxide surfaces at incipient wetness" *J. Colloid Interface Sci*. 1995, 175, 239-252

117. J. S. Noh, J. A. Schwarz. "estimation of the point of zero charge of simple oxides by mass titration" *J. Colliod Interface Sci*. 1989, 130, 157-164

118. G. A. Parks "The isoelectric point of solid oxides, solid hydroxides, and aqueous hydroxo complex systems" *Chem. Rev*. 1965, 65, 177-198

119. R. Fan, S. Huh, R. Yan, J. Arnold, P. Yang. "Gated proton transport in aligned mesoporous silica films" *Nature Mater.* 2008, 7, 303-307

120. S–Y. Chung, J. T. Bloking, Y–M. Chiang. "Electronically conductive phospho-olivines as lithium storage electrodes" *Nature Mater*. 2002, 1, 123-128

121. L. Herlogsson, X. Crispin, N. D. Robinson, M. Sandberg, O–J. Hagel, G. Gustafsson, M. Berggren. "Low-Voltage Polymer Field-Effect Transistors Gated via a Proton Conductor" *Adv. Mater*. 2007, 19, 97-101

122. T. Heimburg, D. Marsh. "Investigation of secondary and tertiary structural changes of cytochrome c in compliexes with anionic lipids using amide hydrogen exchange measurement: an FTIR study" *Biophys. J*. 1993, 65, 2408-2417

123. T. J. T. Pinheiro, G. A. Elöve, A. Watts, H. Roder. "Structural and kinetic description of cytochrome c unfolding induced by the interaction with lipid vesicles" *Biochemistry* 1997, 36, 13122-13132

124. N. Sanghera, T. J. T. Pinheiro. “Unfolding and refolding of cytochrome *c* driven by the interaction with lipid” *Protein Sci.* 2000, 9, 1194-1202

125. M-J. Paquet, M. Laviolette, M. Pézolet, M. Auger. “Two-domensional infrared correlation spectroscopy study of the aggregation of cytochrome c in the presence of dimyristoylphosphatidyglycerol” *Biophys. J*. 2001, 81, 305-312

126. J. O. Speare, T. S. Rush. “IR spectra of cytochrome *c* denatured with deuterated guanidine hydrochloride show increase in β sheet” *Biopolymers (Biospectroscopy),* 2003, 72, 193–204

127. Q. Xu, T. A. Keiderling. “Effect of sodium dodecyl sulfate on folding and thermal stability of acid-denatured cytochrome c: A spectroscopic approach” *Protein Sci.* 2004, 13 , 2949-2959

128. H. Shinohara, M. Grätzel, N. Vlachopoulos, M. Aizawa. “Interfacial electron transfer of flevin coenzymes and riboflavin adsorbed on textured TiO2 films” *Bioelectrochem. Bioenerg.* 1991, 26, 307-320.

129. P. Baglioni, E. Fratini, B. Lonetti, S, H. Chen. “Structural arrest in concentrated cytochrome c solutions: the effect of pH and salts” *J. Phys: Condens.Matter*. 2004, 16, s5003-s5022

130. E. Stellwagen. “Haem exposure as the determinate of oxidation–reduction potential of haem proteins ” *Nature* 1978, 275, 73-74

131. A. J. Bard, L. R. Faulkner. *Electrochemical Methods. Fundamentals and Applications*, 2nd ed.; Wiley: New York, 2001.

132. D. C. Harris *Quantitative Chemical Analysis*, 8nd ed.; W. H. Freeman and Company 2010

133. J. H. Reeves, S. Song, E. F. Bowden. “Application of square wave voltammetry to strongly absorbed quasireversible redox molecules” *Anal.Chem*. 1993, 65, 683-388.

134. X. G. Xu, X. Ding, Q. Chen, L–M. Peng “Modification of electronic, optical, and magnetic properties of titanate nanotubes by metal intercalation” *Phys. Rev. B* 2007, 75, 035423(12)

135. M. D. Hawley, S. V. Tatawawadi, S. Piekarski, R. N. Adams, "Electrochemical Studies of the Oxidation Pathways of Catecholamines" *J. Am. Chem. Soc*. 1967, 89, 447-450.

136. A. Ciszewski, G. Milczarek. " Polyeugenol-Modified Platinum Electrode for Selective Detection of Dopamine in the Presence of Ascorbic Acid" *Anal. Chem*. 1999, 71, 1055-1061.